MAXIMUM ENSTROPHY GROWTH IN BURGERS EQUATION

MAXIMUM ENSTROPHY GROWTH IN BURGERS EQUATION

By

DIEGO AYALA, B.Eng., M.Sc.

A Thesis

Submitted to the school of Graduate Studies

in Partial Fulfilment of the Requirements

for the Degree

of Master of Science

McMaster University

MASTER OF SCIENCE (2010) McMaster University
(Mathematics) Hamilton, Ontario

TITLE:	MAXIMUM ENSTROPHY GROWTH IN BURGERS EQUATION
AUTHOR:	Diego Ayala, B.Eng. (ITESM), M.Sc. (UNAM)
SUPERVISOR:	Dr. Bartosz Protas
NUMBER OF PAGES:	viii, 56

Abstract

It is well known that the regularity of solutions to Navier-Stokes equation is controlled by the boundedness in time of the enstrophy. However, there is no proof of the existence of such bound. In fact, standard estimates for the instantaneous rate of growth of the enstrophy lead to finite time blow up, when straightforward time integration of the estimate is used. Moreover, there is recent numerical evidence to support the sharpness of these instantaneous estimates for any given instant of time. The central question is therefore, how to extend these instantaneous estimates to a finite time interval $(0, T]$ in such a way that the dynamics imposed by the PDE are taken into account.

We state the problem of saturation of finite time estimates for enstrophy growth as an optimization problem, where the cost functional is the total change of enstrophy in a given time interval. We provide an iterative algorithm to solve the optimization problem using Viscous Burgers Equation (VBE) as a "toy" version of Navier-Stokes equation. We give numerical evidence that analytic finite time estimates for enstrophy growth in VBE are conservative, in the sense that they are not saturated.

Acknowledgements

I would like to acknowledge my supervisor Dr. Bartosz Protas, for all his contributions, advice and feedback during the preparation of the present work. I am certain that his guidance has helped me to grow both professionally and personally. In the same spirit, I thank Dr. Dmitry Pelinovsky and Dr. Nicholas Kevlahan for their review of this thesis, and the useful comments following such review.

Contents

List of Figures

Chapter 1

Introduction

As the title indicates, this Thesis is about Burgers Equation. However, the ideas that originated this work are related to one of the fundamental equations of mathematical physics: Navier-Stokes Equation (NSE). The importance of NSE is the product of two factors: on the one hand, engineers and physicists have been using this set of equations to model the dynamics of fluids for more than a century with excellent results, e.g. aerodynamics, hydrodynamics and astrophysics [5]. On the other hand, NSE has eluded the mathematical rigour of proofs for global existence of solutions, which leaves in the air the following question: are solutions to NSE physically reasonable, at least in some sense, for large periods of time? The answer to this question is: we don't know. It is such the importance of this equation that the Clay Mathematics Institute has established a one million dollar prize for anyone who reveals its mathematical mysteries.

To begin our discussion on this topic, consider, for simplicity, $\Omega = [0,1]^3$ to be the domain of definition (this is one of the cases considered by the Clay Mathematics Institute [6]), $\mathbf{u} : \Omega \times [0,\infty) \to \mathbb{R}^3$ be the velocity field and $p : \Omega \times [0,\infty) \to \mathbb{R}$ be the pressure field. Navier-Stokes equation is obtained by a balance of momentum in Newton's second law, and assuming the fluid is incompressible, its complete formulation [4] is given by:

$$\mathbf{u}_t + \mathbf{u} \cdot \nabla \mathbf{u} + \nabla p = \nu \Delta \mathbf{u} \ \text{ in } \Omega \tag{1.1a}$$

$$\nabla \cdot \mathbf{u} = 0 \tag{1.1b}$$

$$\mathbf{u}(\mathbf{x}, 0) = \mathbf{u}_0(\mathbf{x}), \tag{1.1c}$$

where we consider periodic boundary conditions, and the viscosity ν is the only parameter in the model. With the addition of other effects (e.g. external forces, rotation, temperature or electromagnetic coupling) this equation is routinely used to model systems across a large range of length and time scales, from microfluids modelling to oceanography [5].

The proof of existence of solutions for NSE is based on the construction of *weak solutions*. We say that $\mathbf{u}$ is a weak solution to NSE if for any infinitely differentiable, divergence-free test function $\mathbf{v} : \Omega \times [0, \infty) \to \mathbb{R}^3$ with compact support in $t \in [0, \infty)$, and for any smooth $q : \Omega \times [0, \infty) \to \mathbb{R}$ we have [5]:

$$\int_0^\infty \int_\Omega (\mathbf{u} \cdot \mathbf{v}_t + \mathbf{u} \cdot (\nabla \mathbf{v}) \cdot \mathbf{u} + \nu \mathbf{u} \cdot \Delta \mathbf{v}) \, d\mathbf{x} dt = 0 \tag{1.2}$$

and

$$\int_0^\infty \int_\Omega \mathbf{u} \cdot \nabla q \, d\mathbf{x} dt = 0. \tag{1.3}$$

To construct these weak solutions, we start with a regularized approximation to NSE for which global solutions are known, and then consider the limit case as the regularization is removed. In [5], Doering considers a natural regularization coming from the spectral Galerkin approximation to equation (1.1). For fixed positive integer K, let $P_K : L^2(\Omega) \to \ell^2(\mathbb{Z}^3)$ be the projector operator defined as:

$$(P_K \mathbf{u})(x) = \sum_{|\mathbf{k}| \leq K} \hat{u}_\mathbf{k} e^{2\pi i \mathbf{k} \cdot \mathbf{x}}. \tag{1.4}$$

In other words, P_K truncates the Fourier series of $\mathbf{u}$ to spectral components with wave number below K. The Galerkin approximation $\mathbf{u}^K(\mathbf{x}, t) = (P_K \mathbf{u})(\mathbf{x}, t)$ is the solution to the regularized NSE:

$$\frac{\partial \mathbf{u}^K}{\partial t} + P_K \left(\mathbf{u}^K \cdot \nabla \mathbf{u}^K \right) + \nabla p^K = \nu \Delta \mathbf{u}^K \tag{1.5a}$$

$$\nabla \cdot \mathbf{u}^K = 0, \tag{1.5b}$$

with initial data $\mathbf{u}^K(\mathbf{x}, 0) = (P_K \mathbf{u}_0)(\mathbf{x})$. The Fourier coefficients $\hat{u}_\mathbf{k}$ of $\mathbf{u}^K$ satisfy the system of ordinary differential equations [4]:

$$\frac{d\hat{u}_\mathbf{k}}{dt} = -\nu (2\pi |\mathbf{k}|)^2 \hat{u}_\mathbf{k} - 2\pi i \left(1 - \frac{\mathbf{k} \otimes \mathbf{k}}{|\mathbf{k}|^2} \right) \sum_{\mathbf{k}_1 + \mathbf{k}_2 = \mathbf{k}} \hat{u}_{\mathbf{k}_1} \cdot \mathbf{k}_2 \hat{u}_{\mathbf{k}_2} \tag{1.6a}$$

$$\mathbf{k} \cdot \hat{u}_\mathbf{k} = 0, \tag{1.6b}$$

where $1-\mathbf{k}\otimes\mathbf{k}/|\mathbf{k}|^2$ is the projector operator onto divergence-free vector fields. Local unique, bounded and smooth solutions to equation (1.6) follow from the theory of solutions of ordinary differential equations [4, 11]. Moreover, global solutions can be obtained thanks to the a priori bound [5]:

$$\sum_{\mathbf{k}} |\hat{u}_{\mathbf{k}}(t)|^2 \leq \sum_{\mathbf{k}} |\hat{u}_{\mathbf{k}}(0)|^2 = ||\mathbf{u}_0||_2^2. \tag{1.7}$$

At this point, the idea would be to take $K \to \infty$ and look for the convergence of the approximation $\mathbf{u}^K$ to a limit $\mathbf{u}$ that solves NSE. To prove this assertion we would need to show that $\mathbf{u}^K$ constitutes a Cauchy sequence in the space of continuous functions from the interval $[0,T]$ to $L^2(\Omega)$, i.e. we should show that:

$$\lim_{K_1,K_2\to\infty} \sup_{t\in[0,T]} ||\mathbf{u}^{K_1}(\cdot,t) - \mathbf{u}^{K_2}(\cdot,t)||_2 = 0. \tag{1.8}$$

Doering shows in [5] that if there exists a finite real number R such that

$$\int_0^T ||\nabla \mathbf{u}^K(\cdot,t)||_\infty^2 dt < R \tag{1.9}$$

uniformly in K, then we could prove (1.8), where $||f||_\infty = \sup_{\mathbf{x}\in\Omega} |f(\mathbf{x})|$. However, no such uniform bound is known. One important fact worth to keep in mind, is that this uniform bound is not sufficient to establish strong convergence, but it is sufficient to establish the convergence of subsequences of the Galerkin approximation to weak solutions [5].

Another issue with solutions to NSE, besides its existence and uniqueness, is its regularity. If smoothness of solutions is lost on some level, this would indicate the presence of small structures in the flow. A discontinuity implies a "macroscopic" change over a "microscopic" length scale [4]. This phenomena, by itself, should not generate any difficulties. However, the derivation of NSE relies on the smoothness of its solutions to show convergence from the microscopic to the macroscopic scales. For this reason, it is important to monitor the time and length scales involved in the solutions to NSE.

A good way to approach the regularity problem is using the concept of enstrophy. The enstrophy $\mathcal{E}$ is proportional to the square of the L^2 norm of the vorticity $\omega = \nabla \times \mathbf{u}$. For the setting where periodic boundary conditions

are considered, the enstrophy is defined as:

$$\mathcal{E}(t) = \frac{1}{2}\int_{\Omega} |\nabla_x \mathbf{u}(\mathbf{x}, t)|^2 \, d\mathbf{x}. \tag{1.10}$$

It is shown in [4] that the rate of growth of the enstrophy satisfies

$$\frac{d\mathcal{E}}{dt} \leq \frac{c'}{\nu^3}\mathcal{E}^3, \tag{1.11}$$

for large values of enstrophy, where $c' > 0$ is a constant and $\nu > 0$ is the viscosity. A useful regularity criterion can be derived from this inequality. To see this, notice that inequality (1.11) is equivalent to:

$$\frac{d}{dt}\left(\mathcal{E}\exp\left\{\frac{-c'}{\nu^3}\int_0^t \mathcal{E}^2(s)ds\right\}\right) \leq 0, \tag{1.12}$$

meaning that the quantity inside the parenthesis decreases from its initial value. Therefore:

$$\mathcal{E}(t) \leq \mathcal{E}(0)\exp\left\{\frac{c'V(t)}{\nu^3}\right\}, \tag{1.13}$$

where $V(t)$ is defined as:

$$V(t) = \int_0^t \mathcal{E}^2(s)\, ds.$$

If we knew a priori that $V(t)$ is finite for all positive t, we would have regularity of the solutions, since the enstrophy would be bounded for all $t > 0$, meaning that the gradient of the solution $\nabla\mathbf{u} \in L^2$. However, no such bound is known to exist. Moreover, the instantaneous bound given by inequality (1.11) is sharp in the sense that there exist solutions that actually saturate it, as is shown by Lu Lu in his PhD thesis from 2006 [9]. This means that the sequence of estimates used in the derivation of this inequality cannot be improved substantially, but it does not mean that a singularity will develop in finite time. Since inequality (1.11) is of an instantaneous nature, the evolution of the velocity field may drive the flow away from the saturation condition, as in fact the example given by Lu Lu does.

The traditional approach to obtain finite time estimates for the enstrophy is based on the integration over time of instantaneous estimates, like inequality

(1.11). However, for NSE this approach leads to estimates that allow the formation of singularities in finite time (as Doering and Lu show in [10]). Having said this, some questions arise: Is simple integration in time the right way to obtain finite time estimates that take the dynamical properties of the equation into account? Or does it lead to conservative (in the sense of not being sharp enough) estimates?

In the following pages we will address these questions in a computational sense, not for the full three-dimensional Navier-Stokes equation, but for a simpler case in one dimension: Viscous Burgers Equation (VBE). Although existence and uniqueness theory for VBE is a well understood topic (see [8] for an extensive treatment of this issue) and closed form solutions have been found via the Hopf-Cole transformation (as explained in [3]), the question whether sharp finite time estimates for the enstrophy of solutions to VBE can be obtained from sharp instantaneous estimates is still a relevant one.

The structure of this work is as follows: the setup for the problem as well as the fundamental inequalities that will lead to finite time estimates are explained in chapter 2. Chapter 3 contains information regarding adjoint based optimization and the algorithm used to attack the problem. In chapter 4 we present the numerical results and some comments on the validity of our approach. Conclusions and the discussion of the results are presented in chapter 5. Some remarks on the numerical methods used to solve the differential equations and on scaling properties of VBE are made in appendices A and B, respectively.

Chapter 2

Burgers Equation

We can think of Viscous Burgers Equation (VBE) as the one-dimensional (1D) version of Navier-Stokes Equation. Although this idea is not exactly true since the incompressibility condition is taken out from the formulation of VBE, it maintains three important aspects of NSE: the evolution in time, the non linearity and its parabolic nature. For these reasons, Burgers equation has been extensively used as a "workhorse" to test numerical methods and to gain insight in the underlying theory behind the phenomena of fluid motion.

To begin with, let $\Omega = [0, 1]$ be the domain of definition and $u : \Omega \times [0, \infty) \to \mathbb{R}$ be the solution under consideration. Burgers equation is given by:

$$\frac{\partial u}{\partial t} + u\frac{\partial u}{\partial x} - \nu\frac{\partial^2 u}{\partial x^2} = 0 \quad \text{in}\,\Omega \tag{2.1a}$$

$$u(x, 0) = \phi(x). \tag{2.1b}$$

with periodic boundary conditions. Notice that in this case, the incompressibility condition can not be taken into account, since it would lead to trivial constant solutions $u(x, t) = C$. The theory of existence and uniqueness for Burgers equation is extensively covered in [8]. Moreover, it is possible to obtain closed form solutions to Burgers equation. The Hopf-Cole transformation given by

$$u = -2\nu\frac{\psi_x}{\psi} \tag{2.2}$$

reduces equation (2.1) to a heat equation for ψ:

$$\frac{\partial \psi}{\partial t} - \nu \frac{\partial^2 \psi}{\partial x^2} = 0,$$

which can be solved using the Fourier Transform method [3]. However, this approach will not be used in this work, and a numerical method based on spectral approximation will be used instead.

Two important quantities associated to solutions of equation (2.1) are the energy and the enstrophy. The energy is defined as:

$$\mathcal{K}(t) = \frac{1}{2}||u(\cdot,t)||_2^2 = \frac{1}{2}\int_0^1 |u(x,t)|^2 dx, \tag{2.3}$$

whereas the enstrophy is defined as:

$$\mathcal{E}(t) = \frac{1}{2}||u_x(\cdot,t)||_2^2 = \frac{1}{2}\int_0^1 |\partial_x u(x,t)|^2 dx. \tag{2.4}$$

2.1 Instantaneous Bounds for Enstrophy and Energy Growth Rates

It is possible to establish upper bounds for the instantaneous rate of growth (with respect to time) of the enstrophy. Using its definition in equation (2.4) and equation (2.1) we obtain:

$$\begin{aligned} \frac{d\mathcal{E}}{dt} &= \int_0^1 u_x u_{tx} dx = \int_0^1 u_x[(-uu_x)_x + \nu u_{xxx}]dx & (2.5)\\ &= -\nu\int_0^1 (u_{xx})^2 dx + \int_0^1 u u_x u_{xx} dx & (2.6)\\ &= -\nu\int_0^1 (u_{xx})^2 dx - \frac{1}{2}\int_0^1 (u_x)^3 dx, & (2.7) \end{aligned}$$

where integration by parts has been used, and the periodicity of the boundary conditions was used to eliminate the boundary terms. We can now bound the cubic term using the following arguments:

$$\begin{aligned} -\frac{1}{2}\int_0^1 (u_x)^3 dx &= \frac{1}{2}\int_0^1 (-u_x)^3 dx \leq \frac{1}{2}||u_x||_\infty \int_0^1 (-u_x)^2 dx & (2.8)\\ &\leq \frac{1}{2}||u_x||_\infty ||u_x||_2^2. & (2.9) \end{aligned}$$

Using $||f||_\infty \leq C_1||f_x||_2^{1/2}||f||_2^{1/2}$ which can be found in Appendix A of [4], and taking $C_1 = 2\sqrt{\frac{2}{\pi}}$, which is obtained in Appendix B of [9], we get:

$$\frac{d\mathcal{E}}{dt} \leq -\nu||u_{xx}||_2^2 + \sqrt{\frac{2}{\pi}}||u_{xx}||_2^{1/2}||u_x||_2^{5/2}. \tag{2.10}$$

By using Young's inequality

$$ab \leq \frac{1}{2}\left(\frac{\beta^p a^p}{p} + \frac{b^q}{\beta^q q}\right), \ \beta, p, q > 0, \frac{1}{p} + \frac{1}{q} = 1 \tag{2.11}$$

to split the product of $||u_{xx}||_2^{1/2}$ and $||u_x||_2^{5/2}$ we get:

$$\frac{d\mathcal{E}}{dt} \leq -\nu||u_{xx}||_2^2 + \sqrt{\frac{2}{\pi}}\left(\frac{\beta^4||u_{xx}||_2^2}{4} + \frac{3||u_x||_2^{10/3}}{4\beta^{4/3}}\right), \tag{2.12}$$

where we chose $p = 4, q = 4/3$. Taking $\beta^4 = \frac{4\nu\sqrt{\pi}}{\sqrt{2}}$ to cancel the $||u_{xx}||_2^2$ term we obtain:

$$\boxed{\frac{d\mathcal{E}}{dt} \leq \frac{3}{2}\left(\frac{1}{\pi^2\nu}\right)^{1/3}\mathcal{E}^{5/3}}. \tag{2.13}$$

On the other hand, the rate of growth of the energy is given by:

$$\frac{d\mathcal{K}}{dt} = -\nu\int_0^1 (u_x)^2 dx = -\nu||u_x||_2^2 \tag{2.14}$$

which tells us that the energy is a decreasing function of time and it is bounded by the energy of the initial data, i.e.,

$$\mathcal{K}(t) \leq ||u(\cdot,0)||_2^2 = ||\phi||_2^2 \ \forall\, t. \tag{2.15}$$

To obtain an upper bound for the enstrophy we could, naively, integrate inequality (2.13) with respect to time. This approach leads to:

$$\mathcal{E}(t) \leq \frac{\mathcal{E}_0}{(1 - Ct)^{\frac{3}{2}}} \tag{2.16}$$

for some $C > 0$ that depends on the initial enstrophy. Let the right hand side of the last expression be $G(t)$. Then, $\exists\ t^* = 1/C$ such that $\lim_{t\to t^*} G(t) = \infty$.

That is, the inequality is telling us that the enstrophy is upper bounded by some expression that blows up in finite time. However this does not implies that the enstrophy actually blows up.

One could argue that the problem with this "blow up" of the enstrophy has its roots in the analytic estimate we have used. Could it be possible that the scaling of $d\mathcal{E}/dt$ follows a power law with an exponent smaller than that of inequality (2.13)? In that case, the exponent could be such that it prevents the blow up. To give an answer to this question, Lu Lu [9] looks for solutions that saturate this estimate, stating the question as an optimization problem.

2.2 Maximum Growth Rate as an Optimization Problem

In his 2006 PhD thesis (see [9]), Lu Lu addresses the following question: How accurate is the bound for the enstrophy rate of growth, given by inequality (2.13)? The method described in his thesis looks for zero mean solutions u that saturate the instantaneous rate of growth of the enstrophy given by equation (2.7). That is, he solves the following problem:

Problem 1 *Maximize the instantaneous enstrophy growth rate given by:*

$$\frac{d\mathcal{E}}{dt} = -\nu \int_0^1 |u_{xx}|^2 dx - \frac{1}{2}\int_0^1 (u_x)^3 dx$$

subject to

$$\frac{1}{2}\int_0^1 |u_x|^2 dx = \mathcal{E}_0 \quad \textit{and} \quad \int_0^1 u dx = 0.$$

It is quite remarkable that it is possible to find an analytic solution to the problem just stated, and Lu Lu describes how to obtain it. The main ideas are the following: first notice that $d\mathcal{E}/dt$ depends explicitly only on u_x, so it seems natural to define $v = u_x$ and apply the Euler-Lagrange equation to the functional:

$$\mathcal{R}(v) = -\int_0^1 L(x, v, v_x) dx \tag{2.17a}$$

$$L(x, v, v_x) = \nu v_x^2 + \frac{1}{2}v^3 + \frac{\lambda}{2}v^2 + \mu v, \tag{2.17b}$$

where λ and μ are Lagrange multipliers associated to the restrictions

$$\frac{1}{2}\int_0^1 v^2 dx = \mathcal{E}_0 \tag{2.18a}$$

$$\int_0^1 v dx = 0, \tag{2.18b}$$

corresponding to the enstrophy constraint and the zero mean condition, respectively. Lu Lu finds the solution to be:

$$v(x) = (\beta_2 - \beta_3)\mathrm{sn}^2\left(\sqrt{\frac{\beta_1 - \beta_3}{8\nu}}x\right) + \beta_3, \tag{2.19}$$

where sn is the elliptic function of the first kind defined as:

$$\mathrm{sn}(z) = \sin(\theta) \tag{2.20a}$$

$$z(\theta) = \int_0^\theta \frac{dt}{\sqrt{1 - m\sin^2 t}}, \tag{2.20b}$$

and the constants β_1, β_2 and β_3 are given by:

$$\beta_1 = 32\nu K(m)E(m) \tag{2.21a}$$

$$\beta_2 = 32\nu K(m)\left(E(m) - (1-m)K(m)\right) \tag{2.21b}$$

$$\beta_3 = 32\nu K(m)\left(E(m) - K(m)\right). \tag{2.21c}$$

The functions $K(m)$ and $E(m)$ in equation (2.21) are the complete elliptic integrals of the first and second kind, respectively. They are defined as:

$$K(m) = \int_0^1 \left[(1-t^2)(1-mt^2)\right]^{-\frac{1}{2}} dt \tag{2.22a}$$

$$E(m) = \int_0^1 \left[(1-t^2)(1-mt^2)\right]^{\frac{1}{2}} dt \tag{2.22b}$$

and the parameter m is obtained by numerically solving the equation:

$$\frac{1024\nu^2}{3}K^3\left[(2+m)K - 2(1+m)E\right] - 1024\nu^2K^2\left(K-E\right)^2 = 2\mathcal{E}_0, \tag{2.23}$$

where the dependence of K and E on m has been omitted, but is implicit. A plot of the analytic solution of problem 1 obtained by integrating equation

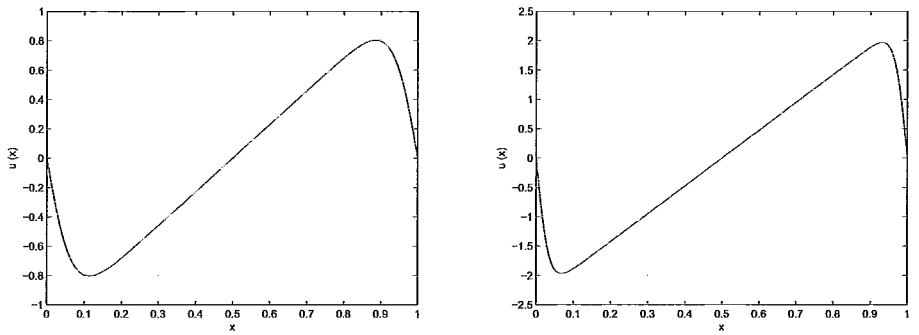

(a) (b)

Figure 2.1: Maximizing solutions of problem 1 with $\nu = 0.01$, corresponding to $\mathcal{E}_0 = 10$ for (a), and $\mathcal{E}_0 = 100$ for (b).

(2.19) is shown in figure 2.1. The values of viscosity and enstrophy are $\nu = 0.01$ and $\mathcal{E}_0 = 10$ for part (a) and $\mathcal{E}_0 = 100$ for part (b).

Once the optimizing solution is found, it is possible to evaluate the maximal rate of growth $d\mathcal{E}/dt$ and provide estimates as $\mathcal{E}_0 \to \infty$. In this case, Lu Lu shows that the maximal rate of growth scales with the same power law as the estimate given by inequality (2.13), that is:

$$\frac{d\mathcal{E}}{dt} \sim \frac{0.2476}{\nu^{1/3}} \mathcal{E}_0^{5/3}, \tag{2.24}$$

meaning that, at least for large values of enstrophy, there are solutions to equation (2.1) that saturate inequality (2.13). At this point, it is worth to discuss an important aspect from the previous result: inequality (2.13) is instantaneous in nature, so solutions that actually saturate it at a particular instant of time, may be driven away from the saturation condition as the solution evolves in time. To validate this idea, consider Viscous Burgers Equation with initial data given by the solution of problem 1, whose plot is shown in figure 2.1 for different values of enstrophy. We keep track of the evolution of the enstrophy as a function of time, and this quantity is shown if figure 2.2, for different values of initial enstrophy $\mathcal{E}_0 \in [10^1, 10^3]$. The plot shows that the enstrophy increases in time up to a maximum value and then decays to zero, for all values of initial enstrophy. Moreover, as shown in figure 2.3, where $\mathcal{E}_{\max} = \max_{t>0} \mathcal{E}(t)$ is plotted as a function of the initial enstrophy $\mathcal{E}_0$, we can

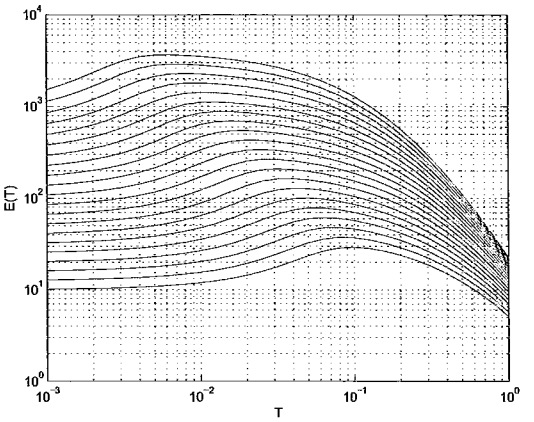

Figure 2.2: Enstrophy as a function of time, for different initial enstrophy.

see it scales as a power law with respect to $\mathcal{E}_0$. Using least squares fitting we find that the exponent associated to the power law is $\alpha \approx 1$. Therefore, as can be seen from the comparison between the exponents $\alpha_0 = 5/3$ from equation (2.24) and $\alpha \approx 1$ from the previous discussion, functions that saturate the instantaneous rate of growth of enstrophy are driven away from the saturation condition, when the dynamics imposed by the time evolution problem are taken into account.

2.3 Finite Time Bound for Enstrophy Growth

Another type of bound, one that considers the possibility of build up of enstrophy within a finite time interval, can be derived using inequality (2.13) and equation (2.14). Integrating in time equation (2.14) we find that:

$$\frac{1}{2\nu}\left[\mathcal{K}_0 - \mathcal{K}(t)\right] = \int_0^t \mathcal{E}(s)ds. \tag{2.25}$$

where $\mathcal{K}_0 = \mathcal{K}(0)$. Since $\mathcal{K}(t) > 0 \; \forall \; t$, we get:

$$\int_0^t \mathcal{E}(s)ds \leq \frac{1}{2\nu}\mathcal{K}_0. \tag{2.26}$$

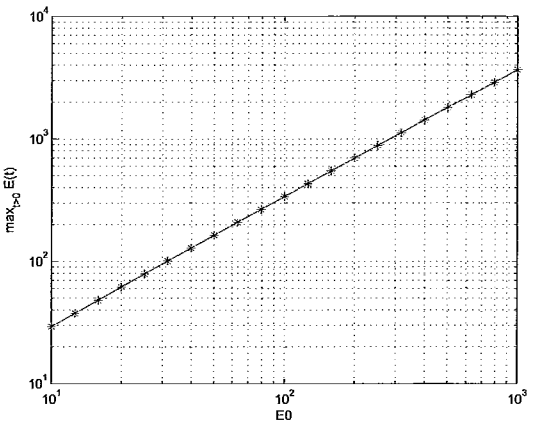

Figure 2.3: Power law with respect to $\mathcal{E}_0$. $\mathcal{E}_{\max} = \max_{t>0} \mathcal{E}(t)$ scales with exponent $\alpha = 1.048$.

Rewriting the right hand side of inequality (2.13) as $C_1 \mathcal{E} \mathcal{E}^{2/3}$, we obtain:

$$3\frac{d}{dt}\mathcal{E}^{1/3} \leq C_1 \mathcal{E}. \tag{2.27}$$

Integration in time leads to:

$$\mathcal{E}^{1/3}(t) - \mathcal{E}_0^{1/3} \leq \frac{C_1}{3}\int_0^t \mathcal{E}(s)ds \leq \frac{C_1}{6\nu}\mathcal{K}_0 \tag{2.28a}$$

$$\leq \frac{C_1}{24\pi^2\nu}\mathcal{E}_0, \tag{2.28b}$$

where the fact that solutions with zero mean are being used allows us to use Poincaré's inequality $\mathcal{K}_0 \leq \frac{1}{4\pi^2}\mathcal{E}_0$ in the last expression. Finally we obtain:

$$\boxed{\mathcal{E}(t) \leq \left[\mathcal{E}_0^{1/3} + \frac{C_1}{24\pi^2\nu}\mathcal{E}_0\right]^3}. \tag{2.29}$$

We summarize this result in the following theorem:

Theorem 1 *Let $\phi \in H^1$ be the initial condition to Burgers equation (2.1). Then its solution $u(\cdot, t) \in H^1 \; \forall \; t$.*

Proof: Follows directly from inequality (2.15) and inequality (2.29). A generalized version if this theorem can be found in [8], where a similar result is shown for H^j, $j \geq 2$.

So far we have seen that for every value of enstrophy, there exist a unique function that saturates the instantaneous rate of growth of the enstrophy $d\mathcal{E}/dt$, and this quantity scales with the enstrophy level as $\mathcal{E}^{5/3}$, as described in section 2.2. However, if we let this function evolve according to the dynamics imposed by VBE, then $\mathcal{E}_{\max} = \max_{t>0} \mathcal{E}(t)$ scales with respect to $\mathcal{E}_0$ as $\mathcal{E}_0^{\alpha}$ for $\alpha \approx 1$.

On the other hand, if inequality (2.29) is sharp, then for large values of initial enstrophy, $\mathcal{E}_{\max}$ should scale as $\mathcal{E}_0^3$. However, the class of functions that saturate the analytic estimate of the instantaneous rate of growth of $\mathcal{E}(t)$ fails to saturate the analytic estimates for finite time. An explanation for this failure is the fact that maximizers of the instantaneous estimate need not to be maximizers of the finite time estimate. In that sense, we should properly state the question of maximum enstrophy growth in finite time.

Having said this, we would like to investigate the existence of functions that saturate the analytic estimate for the maximal enstrophy given as $\mathcal{E}_{\max} \sim \mathcal{E}_0^3$ for large $\mathcal{E}_0$. However, we will look for these functions as the maximizers of the total growth of enstrophy in finite time, for different time intervals. The proper definition of the problem will be stated in chapter 3.

Chapter 3

Saturation of Enstrophy Estimates as an Optimization Problem

Continuing with the discussion from chapter 2, we want to set up the problem of saturation of the estimate $\mathcal{E}_{\max} \sim \mathcal{E}_0^3$ as an optimization problem in the following way: what should be the initial condition $u(x,0)$ with fixed enstrophy $\mathcal{E}_0$ such that, if we let it evolve according to Burgers equation, will allow for the largest increment in enstrophy after some time $T > 0$? Note that in the context of the Clay problem, this formulation would give some insight to the regularity problem since, as mentioned in chapter 1, it is controlled by the boundedness of the enstrophy. In that sense, we would like to find the worst case scenario for the finite time growth of enstrophy, and we would like to see if it is possible for the enstrophy to blow up in finite time. As explained in chapter 2, we do not expect this to happen in the case of Burgers equation, but still is a good exercise to test the accuracy of the analytic estimate.

In this chapter we will cover some issues regarding optimization problems in general, and we will provide an algorithm based on iterative optimization methods to calculate the desired initial condition.

3.1 Statement of Optimization Problem

Optimization and control problems have the following main elements (see [7] for more details):

- Control variables and an associated control space.
- State variables and state space.
- An objective (or cost) functional.
- Constraints that state and control variables must satisfy.

With these four elements, the optimization problem consists in finding the control and state variables that maximize (or minimize) the cost functional, given that both the control variables and the state variables satisfy the imposed constraints.

Regarding the problem we are concerned about, we want to find the initial condition ϕ^* with some prescribed enstrophy $\mathcal{E}_0$ that, evolving in time according to equation (2.1), maximizes the enstrophy at time $t = T$, for fixed T. The total change in the enstrophy during the time interval $[0, T]$ is simply the difference between the enstrophy at time $t = T$ and its value at time $t = 0$. The objective functional is given by:

$$j(\phi, u) = \mathcal{E}(T) - \mathcal{E}(0) = \frac{1}{2}||u_x(\cdot, T)||_2^2 - \frac{1}{2}||\phi_x||_2^2. \tag{3.1}$$

Notice that in the context of optimization theory, the control variable is the initial condition $u(x, 0) = \phi(x)$, while the state variable is the solution to Burgers equation. Also notice that we can represent the restriction imposed by Burgers equation as $G(\phi, u) = 0$. Assuming only local existence and uniqueness of solutions, for any initial condition ϕ there is a unique solution $u(x, t)$ so we can express $u = g(\phi)$, where $g : \chi \to \mathcal{U}$ is the solution operator of Burgers equation, χ is the control space and $\mathcal{U}$ is the state space. Since we want the control variable ϕ to have finite enstrophy, a natural choice is $\chi = H^1$. We can now consider the reduced cost functional

$$\mathcal{J}(\phi) = j(\phi, u(\phi; T)), \tag{3.2}$$

where T is the final time in the definition of $j(\phi, u)$ in equation (3.1). The following is the formal definition of the problem we are interested in solving:

Problem 2 *Given $\mathcal{E}_0$ and T, find the function $\phi^* \in \chi$ such that*

$$\phi^* = \arg\max_{\phi \in \chi} \mathcal{J}(\phi) \qquad \textit{subject to} \quad \frac{1}{2}||\phi_x^*||_2^2 = \mathcal{E}_0$$

for $\mathcal{J}(\phi)$ defined as in equation (3.2).

As usual in constrained optimization problems, we define the augmented cost functional $\mathcal{J}_\lambda(\phi)$ as:

$$\mathcal{J}_\lambda(\phi) = \mathcal{J}(\phi) + \lambda \left(\frac{1}{2}||\phi_x^*||_2^2 - \mathcal{E}_0 \right), \tag{3.3}$$

where λ is the Lagrange multiplier associated to the enstrophy constrain. We say that ϕ^* is a global maximizer if $\phi^* \in \chi$ and:

$$\mathcal{J}(\phi) \leq \mathcal{J}(\phi^*) \ \ \forall\, \phi \in \chi. \tag{3.4}$$

A necessary condition for optimality is:

$$\mathcal{J}'_\lambda(\phi^*; \phi') = 0 \quad \forall\, \phi' \in \chi, \tag{3.5}$$

where $\mathcal{J}'_\lambda(\phi^*; \phi')$ is the Gâteaux derivative of the augmented cost functional, defined as:

$$\mathcal{J}'_\lambda(\phi; \phi') = \lim_{\epsilon \to 0} \frac{\mathcal{J}_\lambda(\phi + \epsilon\phi') - \mathcal{J}_\lambda(\phi)}{\epsilon}. \tag{3.6}$$

A sufficient condition for ϕ^* to be a maximizing solution is that the Hessian associated to the cost functional is a negative definite bilinear form [2]. However, we will not verify this condition, and we will rather use a graphical approach to verify that indeed our method is converging to a maximal solution.

3.2 Iterative Optimization Algorithms

There are two main approaches to solve any optimization problem: the so called *One-Shot* methods, which are based on the Lagrange multipliers method,

Method	Direction of ascent	Notes
Steepest ascent	$d^n = \nabla \mathcal{J}^n$	
Fletcher-Reeves	$d^n = \nabla \mathcal{J}^n - \beta_n^{FR} d^{n-1}$	$\beta_n^{FR} = \frac{\|\|\nabla \mathcal{J}^n\|\|_X^2}{\|\|\nabla \mathcal{J}^{n-1}\|\|_X^2}$
Polak-Ribière	$d^n = \nabla \mathcal{J}^n - \beta_n^{PR} d^{n-1}$	$\beta_n^{PR} = \frac{\left\langle \nabla \mathcal{J}^n, \nabla \mathcal{J}^n - \nabla \mathcal{J}^{n-1} \right\rangle_X}{\|\|\nabla \mathcal{J}^{n-1}\|\|_X^2}$

Table 3.1: Summary of different iterative optimizations methods.

and iterative optimization methods. Since it is very difficult for most problems to find *One-shot* solutions (see [7]), we will focus on the later.

In a general iterative optimization algorithm, we need to find some direction of increase (or decrease if we are interested in minimization problems) of the objective function $\mathcal{J}(\phi)$. Once we have found this direction, we can start up the iterative process which will lead us to a solution, given that we started close (in some sense) to the optimizing solution. Well known optimization algorithms are steepest ascent (descent, in the case of minimization problems), the Fletcher-Reeves method and the Polak-Ribière method [12]. Despite some subtle differences between them, all three are based in the following steps:

- Set $n = 0$, define a tolerance *tol* and start with an initial guess ϕ^n.
- Do
  1. Obtain a direction d^n of increase of the objective function.
  2. Set $\phi^{n+1} = \phi^n + \tau^n d^n$, where $\tau^n = \arg\max_\tau \mathcal{J}(\phi^n + \tau d^n)$.
  3. Evaluate $\Delta\mathcal{J} = (\mathcal{J}(\phi^{n+1}) - \mathcal{J}(\phi^n))/\mathcal{J}(\phi^n)$.
  4. $n \mapsto n + 1$.
- while $\Delta\mathcal{J} > tol$

Different optimization algorithms can be obtained by properly choosing the direction of increase d^n. Table 3.1 shows the values of d^n for the algorithms mentioned above. All cases involve the concept of the gradient $\nabla\mathcal{J}$ of the cost functional, which will be explained in section 3.3. In this work, Polak-Ribière method is used in the solution of problem 2.

3.3 Gradient Extraction

To extract information about the gradient, we will use the cost functional $\mathcal{J}(\phi)$ instead of the augmented cost functional $\mathcal{J}_\lambda(\phi)$, and we will enforce the enstrophy constrain by a procedure that will be explained later in this chapter. Using the definition of the Gâteaux derivative, given by equation (3.6), of the cost functional $\mathcal{J}(\phi)$ defined in equation (3.2) we find that $\mathcal{J}'(\phi;\phi')$ is given by:

$$\mathcal{J}'(\phi;\phi') = \int_\Omega \partial_x u(x,T)\partial_x u'(x,T)dx - \int_\Omega \partial_x\phi(x)\partial_x\phi'(x)dx, \tag{3.7}$$

where $u'(x,t)$ is the solution of the perturbed system (the leading order term in the definition of $\mathcal{J}'$) given by:

$$\partial_t u' + \partial_x(uu') - \nu\partial_x^2 u' = 0 \quad \text{in } \Omega\times[0,T] \tag{3.8a}$$
$$u'(x,0) = \phi'(x) \tag{3.8b}$$
$$\text{Periodic B.C.} \tag{3.8c}$$

Recognizing $\mathcal{J}'(\phi;\phi')$ as a linear bounded functional for $\phi' \in H^1$, by Riesz Representation Theorem [16] there exist $g \in H^1$ such that $\mathcal{J}'(\phi') = \langle g, \phi'\rangle_{H^1}$. We identify g as the gradient $\nabla^{H^1}\mathcal{J}$, and we now look for this gradient.

Integrating equation (3.7) by parts and considering periodic boundary conditions we get:

$$\mathcal{J}'(\phi;\phi') = -\int_\Omega \partial_x^2 u(x,T)u'(x,T)dx + \int_\Omega \partial_x^2\phi(x)\phi'(x)dx. \tag{3.9}$$

Multiplying equation (3.8) by the adjoint variable $u^*(x,t)$ and integrating in both space and time we obtain:

$$\begin{aligned}
0 &= \int_0^T\int_\Omega \left(\partial_t u' + \partial_x(uu') - \nu\partial_x^2 u'\right)u^* dxdt \\
&= \int_\Omega\int_0^T \partial_t u'u^* dtdx + \int_0^T\int_\Omega \partial_x(uu')u^* dxdt - \int_0^T\int_\Omega \nu\partial_x^2 u'u^* dxdt \\
&= \int_\Omega u^*u'\Big|_0^T - \int_0^T\int_\Omega \left(\partial_t u^* + u\partial_x u^* + \nu\partial_x^2 u^*\right)u' dxdt,
\end{aligned}$$

where integration by parts has been used to pass the differential operators from u' to u^*. Setting $\partial_t u^* + u\partial_x u^* + \nu\partial_x^2 u^* = 0$ in the last equation we get:

$$\int_\Omega \phi'(x)u^*(x,0)dx = \int_\Omega u'(x,T)u^*(x,T)dx. \tag{3.10}$$

Setting $u^*(x,T) = -\partial_x^2 u(x,T)$ and substituting in equation (3.9) we get:

$$\mathcal{J}'(\phi;\phi') = \int_\Omega \left[u^*(x,0) + \partial_x^2\phi(x)\right]\phi'(x)dx = \langle \nabla\mathcal{J}, \phi'\rangle_{L^2}. \tag{3.11}$$

The bracketed expression in the last equation refers to the usual inner product in L^2. Up to this point, we have the functional $\mathcal{J}'(\phi')$ represented as the inner product in L^2 between some function $\nabla\mathcal{J}$ and ϕ'. Therefore, the L^2 gradient of the cost functional is given by:

$$\nabla^{L^2}\mathcal{J} = u^*(x,0) + \partial_x^2\phi(x) \tag{3.12}$$

However, $\phi \in L^2$ does not guarantee the required smoothness of the initial condition and, in particular, that its enstrophy will be finite. Since we must satisfy a restriction on the L^2 norm of ϕ_x, we look for a gradient being in a more regular space, i.e. H^1 as mentioned before. In the following section we explain this issue in more detail.

3.4 Gradients in Different Control Spaces

There are two reasons for which we may want to obtain gradients in more regular spaces. The first one, as described at the end of the previous section, refers to the regularity of the functions and the restrictions imposed on certain norms. The second one, is based on the idea that we can accelerate the convergence of the optimization algorithm by choosing the gradient in a suitable function space. This procedure is known as operator preconditioning [15]. In general, we can express the first variation of the cost functional as an inner product in some Hilbert space $\mathcal{V}$. That is:

$$\mathcal{J}'(\phi;\phi') = \left\langle \nabla^{\mathcal{V}}\mathcal{J}, \phi'\right\rangle_{\mathcal{V}} \ \forall\phi' \in \mathcal{V}. \tag{3.13}$$

Let $\mathcal{V} = H^1(\Omega)$ with the usual inner product

$$\langle f, g \rangle_{H^1} = \int_\Omega f\, g + \lambda^2 \frac{\partial f}{\partial x}\frac{\partial g}{\partial x} dx, \tag{3.14}$$

where λ is a length factor that ensures the correct dimensionality of the integral. Taking $f = \nabla^{H^1}\mathcal{J}$ (that is, the gradient in the more regular space $H^1(\Omega)$), $g = \phi'$ (the associated perturbation) and using integration by parts on the second term we get:

$$\left\langle \nabla^{H^1}\mathcal{J}, \phi' \right\rangle_{H^1} = \int_\Omega \left(\nabla^{H^1}\mathcal{J} - \lambda^2 \frac{\partial^2 \nabla^{H^1}\mathcal{J}}{\partial x^2} \right) \phi' dx \tag{3.15}$$

$$= \left\langle \nabla^{L^2}\mathcal{J}, \phi' \right\rangle_{L^2} \tag{3.16}$$

Therefore the H^1 gradient is related to the L^2 gradient via the following equation:

$$\nabla^{H^1}\mathcal{J} - \lambda^2 \frac{\partial^2}{\partial x^2}\nabla^{H^1}\mathcal{J} = \nabla^{L^2}\mathcal{J} \quad \text{in } \Omega \tag{3.17a}$$

$$\text{Periodic B.C.} \tag{3.17b}$$

3.5 The Optimization Algorithm

As stated in sections 3.2 and 3.3 we need to find, at each iteration of the optimization process, the direction of the gradient associated to the first variation of the cost functional. Using equation (3.12) we notice that we need to solve the following two problems:

$$\partial_t u + u\partial_x u - \nu\partial_x^2 u = 0 \quad \text{in } \Omega \times [0, T] \tag{3.18a}$$

$$u(x, 0) = \phi(x) \tag{3.18b}$$

$$\text{Periodic B.C.} \tag{3.18c}$$

$$\partial_t u^* + u\partial_x u^* + \nu\partial_x^2 u^* = 0 \quad \text{in } \Omega \times [0, T] \tag{3.19a}$$

$$u^*(x, T) = -\partial_x^2 u(x, T) \tag{3.19b}$$

$$\text{Periodic B.C.} \tag{3.19c}$$

Equation (3.18) will be referred as the direct problem, and equation (3.19) is known as the adjoint problem. Notice that although the adjoint problem seems to be ill-posed because of the sign on the second spatial derivative, in fact it is well posed, since we are interested in the solution $u^*(x,0)$. Therefore, in this case we deal with a heat type equation in reverse time. The solution to both the direct and adjoint problems is obtained using the pseudo-spectral method described in appendix A. Recalling section 3.3, the L^2 gradient is given by:

$$\nabla^{L^2}\mathcal{J} = u^*(x,0) + \partial_x^2\phi(x) \tag{3.20}$$

whereas the H^1 gradient can be found solving equation (3.17).

Once the direction of increase $d^n = \nabla^{H_1}\mathcal{J}$ has been decided, the updated control variable is given by:

$$\phi^{n+1} = \phi^n + \tau^n d^n, \tag{3.21}$$

where the direction step τ^n is given by:

$$\tau^n = \arg\max_{\tau>0} \left\{\mathcal{J}(\tau) = \mathcal{J}(\phi^n + \tau d^n)\right\}. \tag{3.22}$$

To find τ^n we use Brent's method, an iterative algorithm based on parabolic interpolation to find extrema of functions that requires evaluation of the function itself only, and not of its gradient (see [2] and [14] for details about its implementation).

Moreover, we need to comply with the restriction imposed on the enstrophy of the control variable, which states that it should be equal to a given value $\mathcal{E}_0$. To do this, at every iteration of Brent's method, instead of evaluating the cost functional at $\psi(\tau) = \phi^n + \tau d^n$, we evaluate at the normalized quantity:

$$\tilde{\psi}(\tau) = \frac{\psi(\tau)}{||\psi_x(\tau)||_{L^2}}\mathcal{E}_0 \tag{3.23}$$

which represents the projection of $\psi(\tau)$ on the set $\mathcal{V} = \{\phi \in H^1 : ||\phi_x||_{L^2} = \mathcal{E}_0\}$. This ensures that the control variable has enstrophy $\mathcal{E}_0$ at every iteration of the optimization algorithm. This can be seen as an *arc optimization* over the set $\mathcal{V}$, rather than simply a line optimization along the direction d^n. Figure 3.1 shows a graphical representation of this idea.

A summary of the algorithm is presented in the following lines:

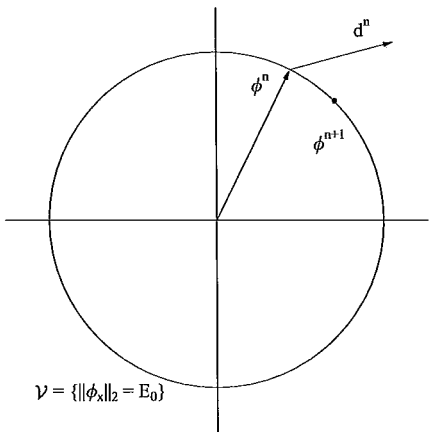

Figure 3.1: Graphical representation of arc optimization. The optimization is performed over the set $\mathcal{V} = \{\phi \in H^1 : \|\phi_x\|_{L^2} = \mathcal{E}_0\}$. The thin line represents the direction of the projection.

1. Set $n = 0$, define a tolerance tol.
2. Set initial guess of control variable ϕ^0.
3. Do
   - Solve the direct problem given by equation (3.18).
   - Solve the adjoint problem given by equation (3.19).
   - Calculate the L^2 gradient with equation (3.12).
   - Calculate the H^1 gradient with equation (3.17).
   - Set $d^n = \nabla \mathcal{J}^n - \beta_n^{PR} d^{n-1}$, β_n^{PR} as given in table 3.1.
   - Find τ^n by performing arc optimization.
   - Set $\phi^{n+1} = \phi^n + \tau^n d^n$.
   - Evaluate $\Delta\mathcal{J} = (\mathcal{J}(\phi^{n+1}) - \mathcal{J}(\phi^n))/\mathcal{J}(\phi^n)$.
   - $n \mapsto n + 1$.
4. while $\Delta\mathcal{J} >$ tol.

Chapter 4

Validation and Results

We provide numerical results to validate the algorithm presented in this work. First, we test the validity of the gradient extraction method described in section 3.3 by performing what is called the *κ-test*. Then, convergence analysis is performed between solutions to Problem 2 defined in chapter 3 and solutions to Problem 1 defined in chapter 2 (i.e. taking the time interval $T \to 0$ in Problem 2). Finally, we present evidence of power laws relating the maximum of enstrophy within a time interval to the value of enstrophy at the beginning of the interval. In all calculations, the numerical solution to both the direct and adjoint problems (as defined in section 3.5) is obtained with the numerical scheme described in appendix A. The tolerance in the optimization algorithm is set to be 10^{-12}. The viscosity in all computations is 10^{-3}, unless otherwise stated.

4.1 Validation of the Gradient

The Gâteaux derivative of any given functional depends on the direction of the perturbation taken into account. Computationally speaking, we are interested in comparing the Gâteaux derivative as the limit given by equation (3.6) with its representation as an inner product between the gradient and the perturbation, once we have used the Riesz Representation Theorem. In other words, we want to be sure that for a wide range of values of ϵ, the following is

satisfied:

$$\frac{\mathcal{J}(\phi+\epsilon\phi')-\mathcal{J}(\phi)}{\epsilon}=\langle\nabla\mathcal{J},\phi'\rangle_{H^1}+\mathcal{O}(\epsilon). \tag{4.1}$$

To compare these two quantities, we plot the quotient

$$\kappa(\epsilon)=\frac{\mathcal{J}(\phi+\epsilon\phi')-\mathcal{J}(\phi)}{\epsilon\langle\nabla\mathcal{J},\phi'\rangle_{H^1}} \tag{4.2}$$

in a log-log axis and observe its behaviour for different values of ϵ. We perform this κ-test for perturbations with different frequency and the results are shown in figure 4.1. In all cases, the control variable is given by $\phi=\sin(2\pi x-\pi)$, whereas the m-th perturbation is set to be $\phi'=\sin(2\pi mx-\pi)$. Notice that for $m=1$, we have $\kappa(\epsilon)=1$ for $\epsilon\in[10^{-11},10^{-3}]$, meaning that we have a good approximation of the gradient. For perturbations of higher frequencies ($m=2,3$ and 4), the range of ϵ for which $\kappa(\epsilon)\approx 1$ is reduced to be $[10^{-9},10^{-5}]$ and $\kappa(\epsilon)$ slightly deviates from 1. This might be due to the non linear nature of the problem, as well as the use of a discrete version of it, that makes some directions difficult to be followed by the gradient. The large deviation from 1 observed in all cases for too large or too small values of ϵ is due to different causes: for large values of ϵ, truncation is the most important source of error, since we are "linearizing" a functional over a subset on which it is non linear. For small values of ϵ, we are faced with round-off errors, due to the finiteness in the precision of the computer used to perform the calculation.

4.2 Arc Optimization and the Cost Functional

Figure 4.2 shows $\mathcal{J}(\tau)=\mathcal{J}(\phi^n+\tau d^n)$ for the first iteration in the optimization algorithm, for different directions d^n. Notice that line optimization along the direction of the gradient allows for larger values of the cost functional, due to the fact that the enstrophy constraint is not being enforced, in contrast with arc optimization, as described in section 3.5. Also, arc optimization gives a smaller value for $\tau^n=\arg\max_{\tau>0}\mathcal{J}(\tau)$. The enstrophy level is $\mathcal{E}=10$ and the time interval is $T=0.1$.

Let ϕ^* be the optimizing solution of problem 2. Figure 4.3 shows the difference between the maximized cost functional $\mathcal{J}(\phi^*)$ and the cost functional at every iteration, normalized with respect to $\mathcal{J}(\phi^*)$, as a function of the iteration for an enstrophy level of $\mathcal{E}_0=100$ and different time intervals. The

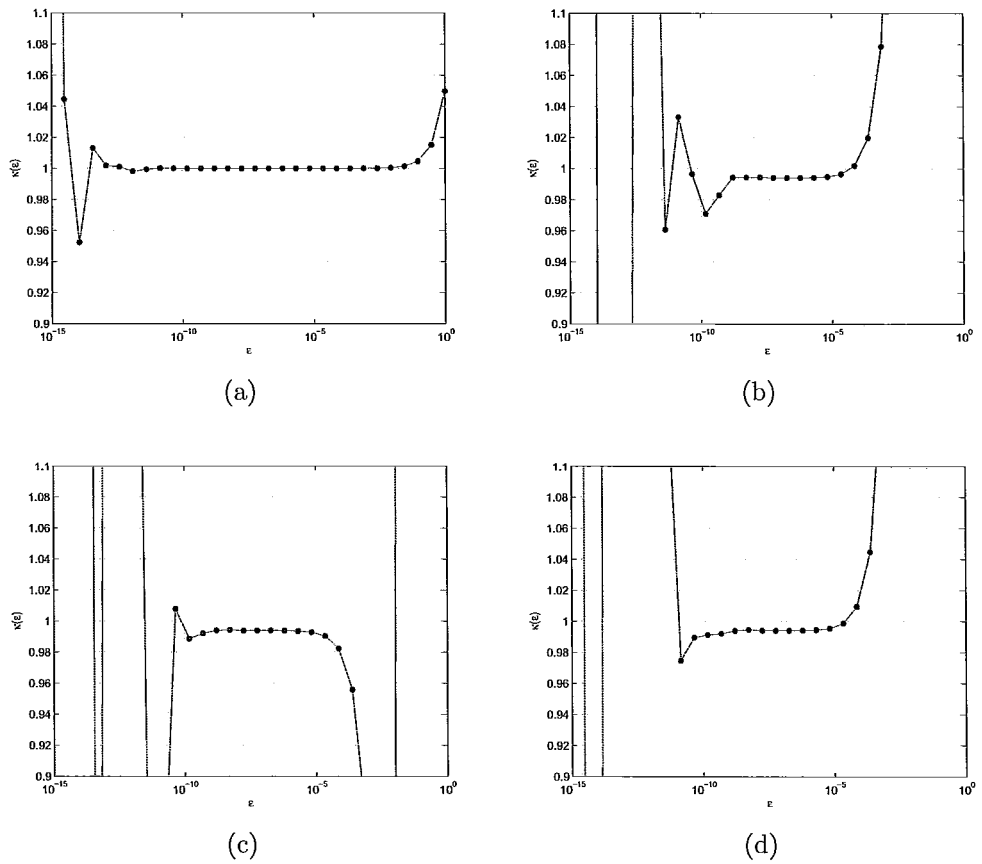

Figure 4.1: The quantity $\kappa(\epsilon)$ for perturbations with different wavenumbers m: (a) $m = 1$, (b) $m = 2$, (c) $m = 3$ and (d) $m = 4$.

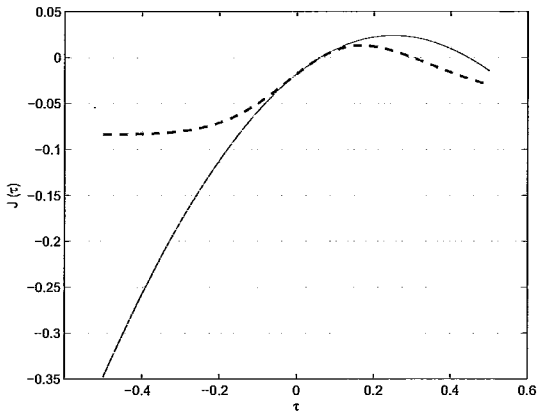

Figure 4.2: Comparison between line optimization along the direction of the gradient (solid line) and arc optimization (dashed thick line). Positive and negative values of τ are shown.

plot is showed in logarithmic scale for the y axis. Notice that the convergence to the optimal value of $\mathcal{J}$ is faster for larger values of the time interval.

4.3 Solution in the Limit $T \to 0$

Referring to the definition of problem 2 in chapter 3, one can expect that as the time interval T tends to 0, solutions to this problem should converge to solutions of problem 1. In other words, if $\phi^*(\cdot\,;T)$ is the solution to problem (2), and ψ is the solution to problem 1 (see equation (2.19)), we would expect that:

$$\lim_{T\to 0} ||\phi^*(\cdot\,;T) - \psi||_p = 0 \tag{4.3}$$

for some norm p. Figure 4.4 shows the square of the L^2 norm of the error between ϕ^* and ψ as a function of the time interval T, normalized with respect to $||\psi||_{L^2}$. The enstrophy level is $\mathcal{E}_0 = 10$ and the viscosity is $\nu = 0.01$. This particularly large value of viscosity (compared to the value we used for the rest of the calculations) was chosen due to the difficulty to numerically evaluate the elliptic integrals and solve, again numerically, equation (2.23) involved in the calculation of ψ. We considered $T \in \{T_n\}_{n=0}^{13}$ with T_n evenly distributed

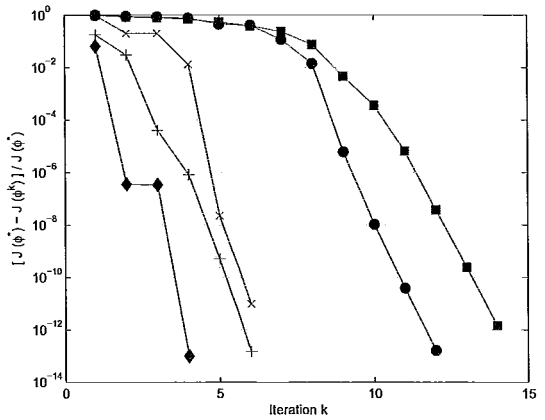

Figure 4.3: The cost functional as a function of the iteration. The cases correspond to: (squares) $T = 10^{-3}$, (circles) $T = 10^{-2}$, ($\times$) $T = 10^{-1.5}$, (+) $T = 10^{-1}$ and (diamonds) $T = 10^{0}$.

in a logarithmic scale between 10^{-6} and 10^{0}. Let ϕ_n^0 be the initial guess used to obtain $\phi^*(T_n)$. We test three different cases:

$$\phi_n^0(x) = \sin(2\pi x - \pi) \ \forall \ T_n \tag{4.4a}$$
$$\phi_n^0(x) = \phi^*(x; T_{n+1}) \tag{4.4b}$$
$$\phi_n^0(x) = \psi(x). \tag{4.4c}$$

Notice from figure 4.4 that the first and second case reach a plateau for $T \approx 10^{-2}$. This may be the effect of having a time interval too short, which does not allows for the algorithm to properly catch the dynamics imposed by the PDE. However, for the third case we observe a monotone decrease on the error as $T \to 0$. If we consider problem 2 as a perturbed version of problem 1, where T, the length of the time interval, is the perturbation parameter, we see that the perturbed solutions $\phi^*(T)$ converge to the unperturbed solution ψ, as long as our initial guess is close enough from ψ.

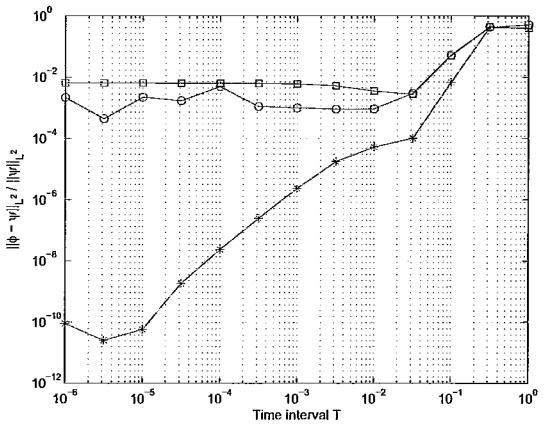

Figure 4.4: Convergence in the L^2 norm of $\phi^*(\cdot;T)$ to ψ, as $T \to 0$. The curves correspond to: (circle) equation (4.4a), (square) equation (4.4b) and (star) equation (4.4c).

4.4 Enstrophy Growth in Finite Time

We are interested in testing the existence of a power law that relates the maximum value of enstrophy given by $\mathcal{E}_{\max} = max_{t>0}\mathcal{E}(t)$ with $\mathcal{E}_0$. To provide numerical evidence of the existence of such power law, we solve the optimization problem 2 for values of time interval $T \in [10^{-3}, 1]$ and values of initial enstrophy $\mathcal{E}_0 \in [10^{-3}, 10^3]$ and obtain $\mathcal{E}(T)$, the enstrophy at the end of the interval $[0, T]$, for every combination of T and $\mathcal{E}_0$. Since the result of the optimization problem may be influenced by the initial guess used in the algorithm, we test different initial guesses, corresponding to different wavenumbers. That is, we use as the initial guess:

$$\phi^0(x) = -A_m \sin(2\pi m x), \tag{4.5}$$

where the amplitude A_m is chosen to enforce the enstrophy restriction, and $m \in \mathbb{N}$. For this particular form of ϕ^0, the initial enstrophy is given by

$$\mathcal{E}_0 = (A_m \pi m)^2, \tag{4.6}$$

and for a given value of $\mathcal{E}_0$ we can calculate the corresponding A_m, for every m.

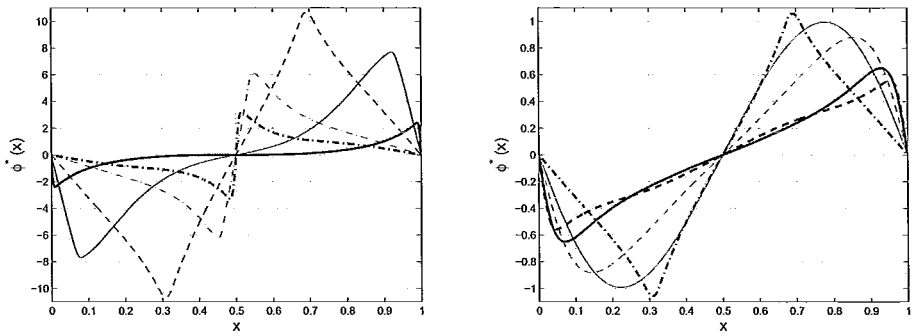

(a) (b)

Figure 4.5: Optimal I.C. for m = 1. (a) Fixed enstrophy $\mathcal{E}_0 = 10^3$ and different time intervals: $T = 10^{-3}$ in solid thick line, $T = 10^{-2}$ in solid thin line, $T = 10^{-1.5}$ in dashed thin line, $T = 10^{-1}$ in dotted thin line and $T = 10^0$ in dotted thick line. (b) Fixed time interval $T = 10^{-1.5}$ and different enstrophy: $\mathcal{E}_0 = 10^{-3}$ for the solid thin line, $\mathcal{E}_0 = 10^{-1.5}$ for the dashed thin line, $\mathcal{E}_0 = 10^0$ for the solid thick line, $\mathcal{E}_0 = 10^{1.5}$ for the dashed thick line and $\mathcal{E}_0 = 10^3$ for the dotted thick line.

4.4.1 Initial Guess with m = 1

We take $m = 1$ in equation (4.5). Solutions to the optimization problem are shown in figure 4.5 for (a) fixed enstrophy $\mathcal{E} = 10^3$, different time intervals and (b) fixed time interval $T = 10^{-1.5}$, different enstrophy. The amplitude of the optimal initial condition (I.C.) ϕ^* showed in part (b) is normalized with respect to the amplitude of the initial guess in the optimization algorithm. Notice in part (a) the change in the shape of ϕ^* as the time interval becomes larger, ranging from solutions shaped like a "shock" wave for small T, to solutions shaped like a "rarefaction" wave for larger T. From part (b) we observe that for small values of initial enstrophy, the optimal I.C. ϕ^* maintains both the shape and the amplitude of the initial guess.

Figure 4.6 shows $\mathcal{E}(T)$ and $\mathcal{E}_{\max} = \max_{t\in[0,T]} \mathcal{E}(t)$ as functions of T in a log-log scale, for different values of initial enstrophy, with $\mathcal{E}_0$ increasing from bottom to top. In this definition $\mathcal{E}_{\max}$ depends on the value of the time interval T. It is worth to point out that $\mathcal{E}_{\max}$ is not far from $\mathcal{E}(T)$ for small values of T,

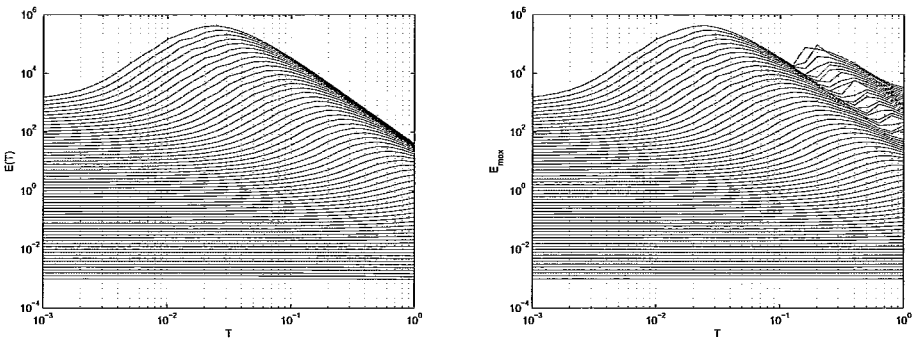

(a) (b)

Figure 4.6: m = 1. (a) Final enstrophy $\mathcal{E}(T)$ as a function of time interval for different initial enstrophy. (b) $\mathcal{E}_{\max}$ as a function of the time interval, for different initial enstrophy.

even for larger values of $\mathcal{E}_0$, meaning that for every choice of T, $\mathcal{E}_{\max}$ is attained at (or close to) the end of the interval $[0, T]$. The plot also indicates that for large time intervals and higher values of initial enstrophy, the maximum of the enstrophy is considerably larger than the enstrophy at the end of the interval, so $\mathcal{E}(T) \ll \mathcal{E}_{\max}$.

Figure 4.7 shows $\mathcal{E}(T)$ and $\mathcal{E}_{\max}$ now as a function of the initial enstrophy in a log-log scale, for different values of T. Notice the formation of an envelope given by:

$$\tilde{\mathcal{E}} = \max_T \{\mathcal{E}_{\max}\}. \tag{4.7}$$

It can be appreciated a linear scaling of the envelope $\tilde{\mathcal{E}}$ with respect to large values of $\mathcal{E}_0$, in the log-log plot. This indicates that the envelope may obey a power law of the form:

$$\tilde{\mathcal{E}} = C_1 \mathcal{E}_0^{\alpha}. \tag{4.8}$$

As shown in figure 4.6, for large values of $\mathcal{E}_0$ there is a time interval $T_{\max}$ such that $\mathcal{E}(T_{\max}) = \max_T \mathcal{E}_{\max}$. As can be seen in figure 4.8 part (b), $T_{\max} = \arg\max_T \mathcal{E}_{\max}$ also follows a power law of the form:

$$T_{\max} = C_2 \mathcal{E}_0^{\beta}. \tag{4.9}$$

Figure 4.8 shows $\tilde{\mathcal{E}}$ and $T_{\max}$ as functions of $\mathcal{E}_0$. The figure also shows the

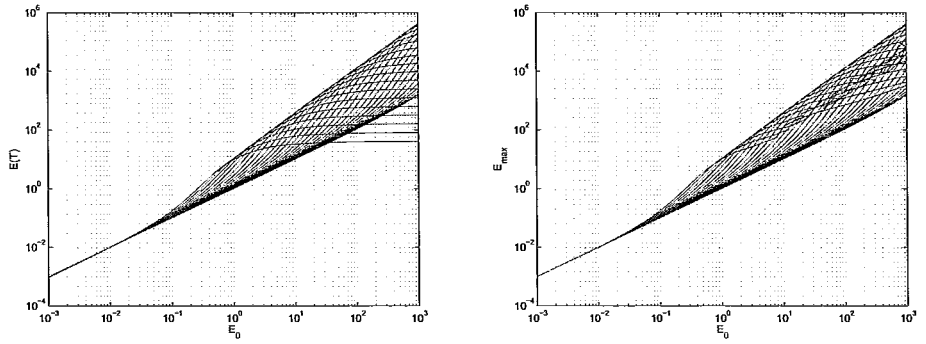

(a) (b)

Figure 4.7: m = 1. (a) Final enstrophy $\mathcal{E}(T)$ as a function of initial enstrophy for different time intervals. (b) $\mathcal{E}_{\max}$ as a function of the initial enstrophy, for different time intervals.

power fit (linear in the logarithmic scale) obtained by least squares. The corresponding exponents are $\alpha \approx 1.5$ and $\beta \approx -0.5$.

4.4.2 Initial Guess with Higher Wavenumber

We would like to be sure that the optimization algorithm described in section 3.5 gives a global optimizer. To do this, we take different wavenumbers m in the initial guess of the algorithm. Here are shown the results for $m = 2$ in equation 4.5. The solutions to the optimization problem for different time intervals and fixed $\mathcal{E}_0$ are shown in figure 4.9. These optimal I.C. seem to be rescaled copies of the corresponding solutions for $m = 1$, and there is strong evidence that shows that in fact, they are. As shown in appendix B, if ϕ_1 and ϕ_2 are used as initial conditions in Burgers equation, and they are scaled versions of each other, then there exists a rescaling of the variables (x, t) such that the corresponding solutions will satisfy the same scaling as ϕ_1 and ϕ_2. In this context, if we define $L = m_2/m_1$ with m_1 and m_2 the corresponding dominant wavenumbers of ϕ_1 and ϕ_2, then the enstrophy level and the time interval scale as $\mathcal{E}_2 = L^4\mathcal{E}_1$ and $T_2 = T_1/L^2$, respectively.

Figure 4.10 shows the optimal initial conditions for wavenumbers $m_1 = 1$ and $m_2 = 2$. The enstrophy level and time interval are $\mathcal{E}_1 = 100$ and $T = 0.1$

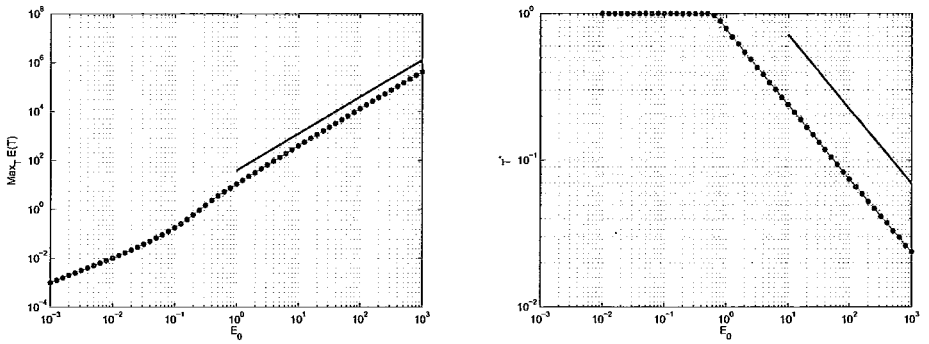

(a) (b)

Figure 4.8: m = 1. (a) $\tilde{\mathcal{E}}$ and fitted power law as function of initial enstrophy. The exponent in the power law is $\alpha = 1.525$. (b) $T_{\max}$ and fitted power law as function of initial enstrophy. The exponent in the power law is $\beta = -0.5109$.

for m_1, and, by the scaling mentioned above, $\mathcal{E}_2 = 1600$ and $T = 0.025$ for m_2. It can be noticed that the solutions to the optimization problem agree with each other once the rescaling is applied. Hence, we will focus only on solutions with dominant wavenumber $m = 1$.

4.4.3 Initial Guess Combining Different Wavenumbers

So far we have started the optimization problem with an initial guess of a single wavenumber. To include more general functions, we consider an initial guess of the form:

$$\phi^0(x) = A_{m_1} \sin(2\pi m_1 x - \pi) + A_{m_2} \sin(2\pi m_2 x - \pi) \tag{4.10}$$

where A_{m_1} and A_{m_2} are chosen so ϕ^0 satisfies the enstrophy constraint, once m_1 and m_2 have been defined. For this choice of ϕ^0, the initial enstrophy is given by

$$\mathcal{E}_0 = (A_{m_1}\pi m_1)^2 + (A_{m_2}\pi m_2)^2, \tag{4.11}$$

so for a given value of $\mathcal{E}_0$ we can choose A_{m_1} and A_{m_1} and enforce the enstrophy constraint.

For simplicity, we choose $m_1 = 1$ and $m_2 = 2$. On a first calculation we define A_1 and A_2 to satisfy $A_1 + A_2 = 1$, i.e. the initial guess is a convex

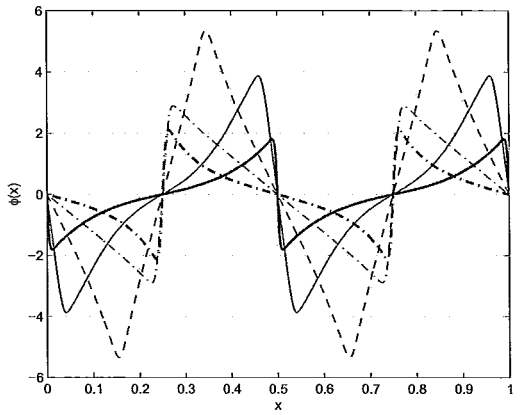

Figure 4.9: Optimal I.C. for $m = 2$, for different time intervals: $T = 10^{-3}$ in solid thick line, $T = 10^{-2}$ in solid thin line, $T = 10^{-1.5}$ in dashed thin line, $T = 10^{-1}$ in dotted thin line and $T = 10^{0}$ in dotted thick line.

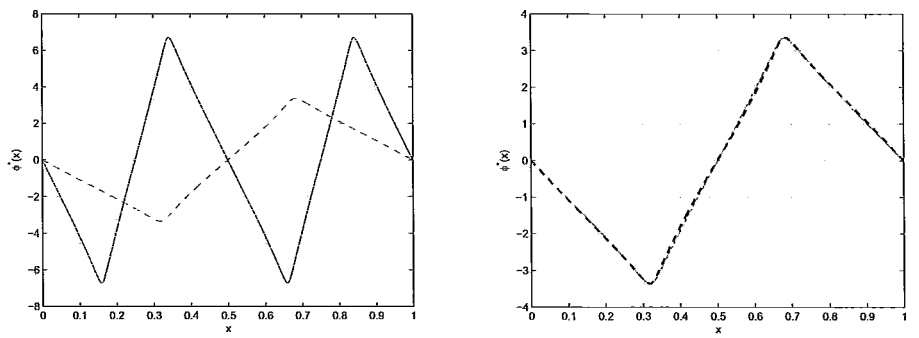

(a) (b)

Figure 4.10: (a) Optimal initial conditions for wavenumbers $m_1 = 1$ (dashed) and $m_2 = 2$ (solid). (b) Rescaling of the two functions in the interval $[0, 1]$.

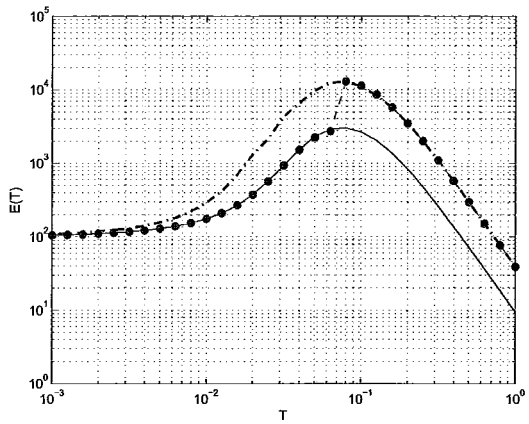

Figure 4.11: $\mathcal{E}(T)$ for a convex linear combination of sine waves with different wavenumber, as the initial guess (dotted line). The solid line corresponds to $\mathcal{E}(T)$ for $\phi^0(x) = A_2 \sin(4\pi x - \pi)$ and the dashed line corresponds to $\phi^0(x) = A_1 \sin(2\pi x - \pi)$.

combination of $\sin(2\pi x)$ and $\sin(4\pi x)$. Figure 4.11 shows the final enstrophy $E(T)$ as a function of the time interval T, with $\mathcal{E}_0 = 100$. As can be seen for this particular initial guess, $\mathcal{E}(T)$ seems to be on either the curve corresponding to the case $m = 2$ for small values of T or on the curve corresponding to $m = 1$ for large values of T.

In general we should not expect any special relation between A_1 and A_2, except for them to ensure the enstrophy constraint, so we performed the calculation for different combinations of A_1 and A_2 within some range. The results are shown in figure 4.12, for initial enstrophy $\mathcal{E}_0 = 100$. In this case, the curve associated to each combination seems to be closer to the curve corresponding to $A_2 = 0$. This result, and the discussion related to figure 4.11 seem to indicate that to consider initial guesses with two or more wavenumbers, it might be enough to focus on the single wavenumber cases. However, this should be carefully tested in future simulations.

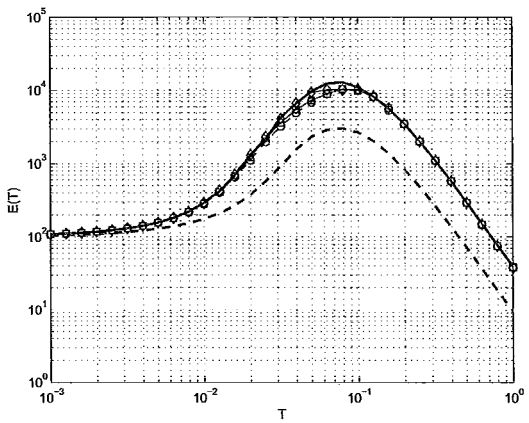

Figure 4.12: $\mathcal{E}(T)$ for a linear combination of sine waves with different wavenumber. The values of the amplitudes are the following: $A_1 = 0.0$ and $A_2 = 1.5915$ (dashed thick line); $A_1 = 0.7958$ and $A_2 = 1.541$ (circles), $A_1 = 1.5915$ and $A_2 = 1.3783$ (squares), $A_1 = 2.3873$ and $A_2 = 1.0527$ (diamonds), $A_1 = 3.1831$ and $A_2 = 0$ (solid thick line).

Chapter 5

Discussion, Conclusions and Future Work

Having at hand the numerical evidence presented in chapter 4, we return to the question: is the finite time analytic estimate for the enstrophy accurate? To give an answer to it, consider the following quantities:

$$T_{\max} = \arg\max_{t} \left\{ \max_{t>0} \mathcal{E}(t) \right\} \tag{5.1a}$$

$$\mathcal{E}_{\max} = \mathcal{E}(T_{\max}). \tag{5.1b}$$

Notice that, by definition, $\mathcal{E}(t) \leq \mathcal{E}_{\max} \; \forall \; t > 0$, so it is enough to verify if $\mathcal{E}_{\max}$ saturates inequality (2.29). As discussed in chapter 4, $\tilde{\mathcal{E}} = \mathcal{E}_{\max}$ satisfies a power law for large values of $\mathcal{E}_0$. From this power laws we can conclude that inequality (2.29) is far from being sharp. Indeed, notice that for large values of initial enstrophy, the power law from inequality (2.29) scales as $\mathcal{E}_0^3$, whereas $\mathcal{E}_{\max}$ scales as $\mathcal{E}_0^{\alpha}$ for $\alpha \approx 1.5$.

In other words, the finite time analytic estimate indicates that $\mathcal{E}_{\max}$ should scale as $\mathcal{E}_0^3$, and as shown in chapter 2, if we use the functions that saturate the instantaneous estimate as the initial condition in VBE we obtain a scaling of $\mathcal{E}_{\max}$ as $\mathcal{E}_0^{\alpha_1}$ for $\alpha_1 \approx 1$. Moreover, by solving problem 2 we found solutions for which $\mathcal{E}_{\max}$ scales as $\mathcal{E}_0^{\alpha_2}$ for $\alpha_2 \approx 1.5$. However, this scaling is still far from saturate the analytic estimate. Figure 5.1 shows the different power laws just discussed.

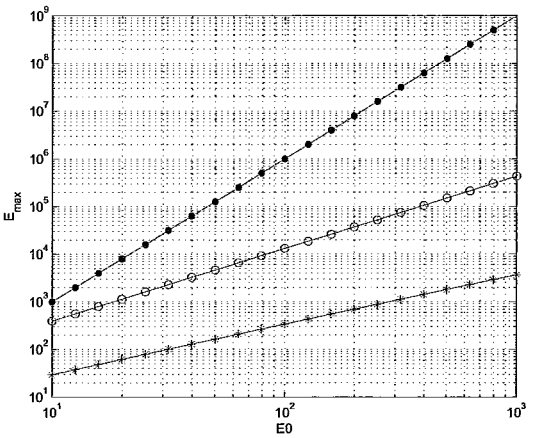

Figure 5.1: Power laws for $\mathcal{E}_{\max}$ considering different situations: the analytic estimate with exponent $\alpha = 3$ (dots); I.C. given by the optimizer of the instantaneous estimate with exponent $\alpha_1 = 1.048$ (stars) and I.C. given by the optimizer of the finite time estimate with exponent $\alpha_2 = 1.525$ (circles).

At this point, we are in position to discuss the difference in the analytic estimate and the one obtained numerically. Notice that in the derivation of estimate (2.29), we used an intermediate inequality to obtain an upper bound for the term involving the integral of the enstrophy. Referring to section 2.3, we used:

$$\int_0^t \mathcal{E}(s)ds \leq \frac{1}{2\nu}\mathcal{K}_0. \tag{5.2}$$

If we use the exact value of the integral of the enstrophy instead, i.e. equation (2.25), we would end up with:

$$\mathcal{E}^{1/3}(t) - \mathcal{E}_0^{1/3} \leq \frac{C_1}{3}\int_0^t \mathcal{E}(s)ds = \frac{C_1}{6\nu}[\mathcal{K}_0 - \mathcal{K}(t)]. \tag{5.3}$$

The main difference between this last inequality and the already discussed bound for the enstrophy is that we do not know, *a priori*, how the difference in the energy levels scales with the initial enstrophy. If we knew that

$$\mathcal{K}_0 - \mathcal{K}(t) \sim \mathcal{E}_0^{\gamma} \tag{5.4}$$

for some $0 < \gamma < 1$, we could obtain a better estimate for inequality (2.29) depending on the value of γ. Notice that the analytic estimate assumes the

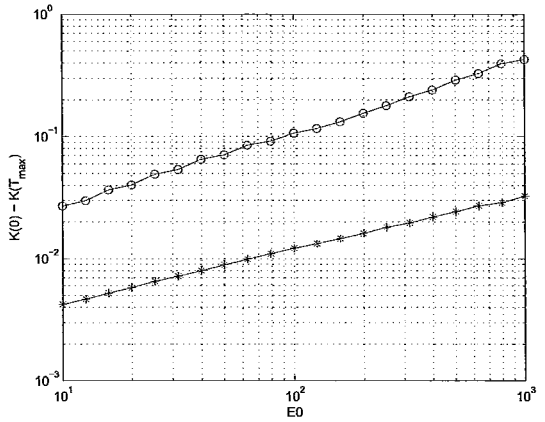

Figure 5.2: Difference in energy levels $\mathcal{K}_0 - \mathcal{K}(T_{\max})$ as a function of $\mathcal{E}_0$. The exponents of the power laws are $\gamma_1 = 0.4422$ for the optimizers of instantaneous estimate as I.C. (stars) and $\gamma_2 = 0.5982$ for solutions to finite time optimization problem as I.C. (circles).

value $\gamma = 1$. Figure 5.2 shows $\mathcal{K}_0 - \mathcal{K}(T_{\max})$ as a function of the initial enstrophy $\mathcal{E}_0$, where $T_{\max}$ as defined in equation (5.1). Using least squares fitting, we find that $\gamma \approx 0.6$, which gives a more accurate *a posteriori* estimate for the difference in energy levels, hence a better approximation for the integral of the enstrophy over the time interval. This is, in our opinion, where the analytic estimate ceases to be sharp and overestimates the enstrophy growth. For comparison purposes, the figure also includes $\mathcal{K}_0 - \mathcal{K}(T_{\max})$ for the case where the initial condition is the function obtained by Lu as the solution of problem 1.

Figure 5.3 shows the energy of the solutions of problems 1 (instantaneous estimate) and 2 (finite time estimate) as a function of the enstrophy, for two different instants of time: time $t = 0$ in part (a), and time $t = T_{\max}$ in part (b). Notice that the solutions associated to the finite time estimate problem are closer to satisfy Poincaré inequality $\mathcal{K}(t) \leq C\mathcal{E}(t)$, compared to solutions associated to the instantaneous estimate problem. This can be observed from the value of the exponent of the power law for each case: $\eta_1, \theta_1 \approx 0.7$ for solutions to problem 1, and $\eta_2, \theta_2 \approx 1$ for solutions to the finite time estimate problem.

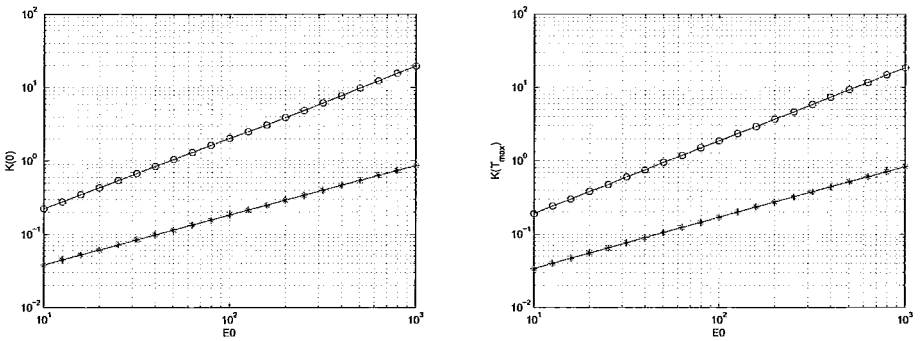

(a) (b)

Figure 5.3: Energy as a function of enstrophy. (a) $\mathcal{K}(0)$ vs $\mathcal{E}_0$. The exponents of the power laws are $\eta_1 = 0.6774$ for solutions to the instantaneous optimization problem (stars) and $\eta_2 = 0.9683$ for solutions to finite time optimization problem (circles). (b) $\mathcal{K}(T_{\max})$ vs $\mathcal{E}_0$: the corresponding exponents are $\theta_1 = 0.6944$ and $\theta_2 = 0.9907$.

Finally, table 5.1 summarizes all the power laws we have presented so far. For solutions to both the instantaneous and finite time estimate optimization problems we have obtained $\mathcal{E}_{\max} \sim \mathcal{E}_0^{\alpha_j}$, $T_{\max} \sim \mathcal{E}_0^{\beta_j}$, $\mathcal{K}(0) \sim \mathcal{E}_0^{\eta_j}$, $\mathcal{K}(T_{\max}) \sim \mathcal{E}_0^{\theta_j}$ and $\mathcal{K}(0) - \mathcal{K}(T_{\max}) \sim \mathcal{E}_0^{\gamma_j}$, where the index j in the exponent of the power law corresponds to the instantaneous ($j = 1$) or the finite time ($j = 2$) cases.

From the information in this table, we can conclude that:

1. Functions that saturate the instantaneous estimate of the enstrophy growth do not saturate the analytic finite time estimate.

2. By setting up the right optimization problem, i.e. including time evolution, we find functions for which we obtain a larger enstrophy growth, but still the analytic finite time estimate is far from being saturated.

3. *A posteriori* calculations show that the analytic bound on enstrophy growth may be overestimating the decrease in the energy, and that might be the reason for solutions of the finite time optimization problem of being far from saturating the analytic estimate.

4. Solutions to the finite time optimization problem are closer to saturate

	Instantaneous optimization problem	Finite time optimization problem
$\mathcal{E}_{\max}$	$\alpha_1 \approx 1$	$\alpha_2 \approx 1.5$
$T_{\max}$	$\beta_1 \approx -0.6$	$\beta_2 \approx -0.5$
$\mathcal{K}(0)$	$\eta_1 \approx 0.7$	$\eta_2 \approx 1$
$\mathcal{K}(T_{\max})$	$\theta_1 \approx 0.7$	$\theta_2 \approx 1$
$\mathcal{K}(0) - \mathcal{K}(T_{\max})$	$\gamma_1 \approx 0.45$	$\gamma_2 \approx 0.6$

Table 5.1: Summary of power laws for the two problems: instantaneous estimate and finite time estimate.

Poincaré inequality than solutions to the instantaneous optimization problem.

Regarding further work along the lines exposed in this thesis, we want to study the more general setting of Navier-Stokes equation, where we would try to establish the same type of power laws and investigate if any of the inequalities presented in the introduction is saturated or not. This could, in turn, provide some insight to the existence and uniqueness problem that has been so elusive for so many years.

Appendix A

Pseudo-Spectral Method

The solutions to the direct and adjoint problems given by equations (3.18) and (3.19) respectively, are obtained numerically using a pseudo-spectral approach (see [3] and [17] for more details). For consistency purposes, both equation are stated one more time. The direct problem refers to the solution of Burgers equation, given by:

$$\partial_t u + u\partial_x u - \nu\partial_x^2 u = 0 \quad (x,t) \in [0,1] \times [0,T] \tag{A.1a}$$

$$u(x,0) = \phi(x) \tag{A.1b}$$

$$\text{Periodic B.C.}, \tag{A.1c}$$

while the adjoint problem is the following linear (in the adjoint variable u^*) equation:

$$\partial_t u^* + u\partial_x u^* + \nu\partial_x^2 u^* = 0 \quad (x,t) \in [0,1] \times [0,T] \tag{A.2a}$$

$$u^*(x,T) = -\partial_x^2 u(x,T) \tag{A.2b}$$

$$\text{Periodic B.C.} \tag{A.2c}$$

The periodic boundary conditions suggest that we should use complex exponentials as our fundamental basis. To begin with, we state the direct problem in terms of Fourier components. If $u(x,t)$ is a solution, then we decompose it as:

$$u(x,t) = \sum_{k\in\mathbb{Z}} \hat{u}_k(t) e^{2\pi i k x} \tag{A.3}$$

Substituting this expression in Burgers Equation, we get for every mode in the Fourier expansion:

$$\frac{d\hat{u}_k(t)}{dt} = -\nu(2\pi k)^2 \hat{u}_k - \widehat{(uu_x)}_k \quad k \in \mathbb{Z} \tag{A.4}$$

To solve the problem numerically, we consider only a finite number of Fourier modes. In our case, $N = 1024$ modes were considered, and $k \in [-N/2+1, N/2]$. Notice that, after discretizing, we end up with a system of N ordinary differential equations that can be written as:

$$\mathbf{y}' = A\mathbf{y} + \mathbf{r}(\mathbf{y}) \tag{A.5}$$

where A is a linear diagonal operator and $r : \mathbb{R}^N \to \mathbb{R}^N$ is a nonlinear map. It is worth to mention that the non linear term in this equation will not be treated completely in the spectral space. Instead, all products of functions are performed in real space (thus avoiding the calculation of convolutions) and then transformed to the spectral space. This gives the method its "pseudo-spectral" character. In the calculation of products in real space, the "3/2" dealiasing rule described in [13] is used. The parabolic nature of the equation calls for the use of an implicit time marching scheme, to avoid the need of using time steps restrictively small. However, fully implicit methods are difficult to implement on non-linear problems, so we use a semi-implicit scheme. The integration in time is performed using a combined Runge-Kutta (explicit for the nonlinear part) and Crank-Nicolson (implicit for the linear part) method given by:

$$\left(I - \frac{4\Delta t}{15}A\right)\mathbf{y}^1 = \left(I + \frac{4\Delta t}{15}A\right)\mathbf{y}^n + \frac{8\Delta t}{15}\mathbf{r}(\mathbf{y}^n) \tag{A.6a}$$

$$\left(I - \frac{\Delta t}{15}A\right)\mathbf{y}^2 = \left(I + \frac{\Delta t}{15}A\right)\mathbf{y}^1 + \frac{5\Delta t}{12}\mathbf{r}(\mathbf{y}^1) - \frac{17\Delta t}{60}\mathbf{r}(\mathbf{y}^n) \tag{A.6b}$$

$$\left(I - \frac{\Delta t}{6}A\right)\mathbf{y}^{n+1} = \left(I + \frac{\Delta t}{15}A\right)\mathbf{y}^2 + \frac{1\Delta t}{6}\mathbf{r}(\mathbf{y}^2) - \frac{17\Delta t}{60}\mathbf{r}(\mathbf{y}^1) \tag{A.6c}$$

where $\mathbf{y}^{n+1}$ and $\mathbf{y}^n$ are the solutions at time step $n+1$ and n respectively. It is worth to mention that, although the restriction imposed by the diffusive term on the size of the time step has been eliminated by the use of the implicit part of the numerical scheme, we still have a strong restriction for Δt due to the presence of the convective term uu_x. In order for the numerical method to be

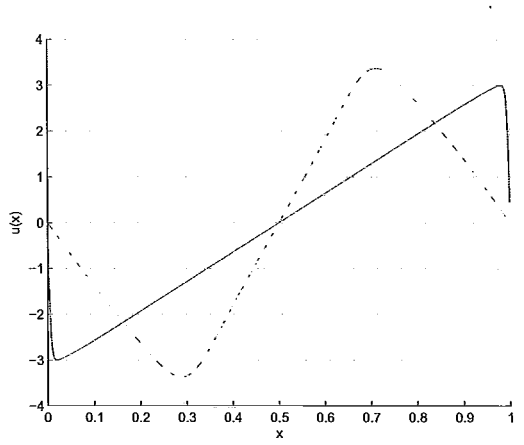

Figure A.1: Solution to direct problem using RK3-CN method. The plot shows both the initial condition (dashed line) and the solution for t=T (solid line).

stable, it should satisfy the CFL condition $U\frac{\Delta t}{\Delta x} \leq 1$, for $U = \max_{x\in\Omega} u(x,0)$, thus imposing an upper bound for the time step [3]. For more details on the derivation of method (A.6) see [1]. We will refer to this method as RK3-CN.

The numerical solution of equation (A.2) is obtained following the same idea of discretizing in Fourier space. The associated ODE is given by:

$$\frac{d\widehat{(u^*)}_k(t)}{dt} = \nu(2\pi k)^2\widehat{(u^*)}_k - \widehat{(uu_x^*)}_k \quad k \in [-N/2+1, N/2] \tag{A.7}$$

and it is integrated in time using the RK3-CN algorithm described before, where the term $\widehat{(uu_x^*)}$ is treated as the nonlinear term in equation (A.6). Notice that even though is a linear term, its evaluation requires, $\forall\ t \in [0,T]$, the storage of the velocity field u obtained as the solution of the direct problem. For large time intervals, this becomes a very expensive expression in terms of computer memory.

Solutions of the two systems are shown in figures A.1 and A.2. The enstrophy of the initial condition is $\mathcal{E}_0 = 100$ and the time window is $T = 0.1$. The initial condition used in the direct problem is the optimizing solution for these particular values of entrophy and time window. The viscosity is $\nu = 0.01$.

To test the accuracy of the pseudo-spectral method, we compare the numerical solution with the exact solution obtained using the Hopf-Cole transfor-

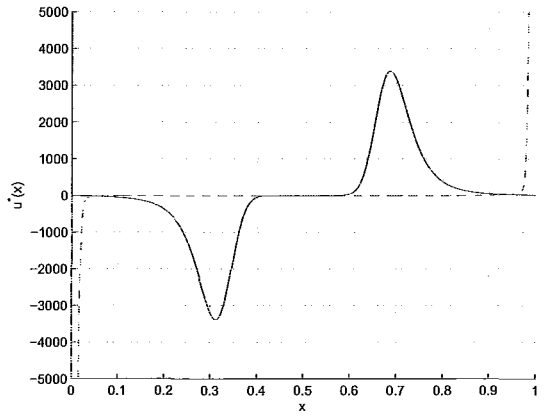

Figure A.2: Solution to the adjoint problem using RK3-CN method. The plot shows both the initial (t=T) condition (dashed line) and the solution for t=0 (solid line).

mation, as described in chapter 2, equation (2.2). To use this transformation, we proceed as follows: given $u(x,0) = \phi(x)$ as the initial condition for Burgers equation, we obtain $\psi(x,0)$ as:

$$\psi(x,0) = \exp\left\{-\frac{1}{2\nu}\int_0^x \phi(\xi)d\xi\right\}, \tag{A.8}$$

and we let it evolve in time according to the heat equation. Using Fourier decomposition we let $\psi(x,t) = \sum_{k\in\mathbb{Z}} \hat{\psi}_k(t)e^{2\pi ikx}$. Then the Fourier coefficients $\hat{\psi}_k(t)$ are given by:

$$\hat{\psi}_k(t) = \hat{\psi}_k(0)e^{-\nu(2\pi k)^2 t} \tag{A.9}$$

where $\hat{\psi}_k(0)$ corresponds to the Fourier coefficients of the initial data $\psi(x,0)$. Hence, we can evaluate $\psi(x,t)$ and obtain $u(x,t)$ using equation (2.2). Figure A.3 shows the square of the L^2 norm of the relative error of the numerical solution with respect to the exact solution, for different spatial step size h. The initial condition is $u(x,0) = \sin(2\pi x)$. In theory, the order of accuracy should be $\mathcal{O}(\Delta t^2 + e^{\alpha h})$ where the exponential term refers to spectral accuracy. However, since the method must satisfy a Courant-type condition of the form $\Delta t \leq h/U$, U as described before, we have $\Delta t \sim h$. Therefore, the order of accuracy ends up being $\mathcal{O}(h^2)$, as can be appreciated in figure A.3.

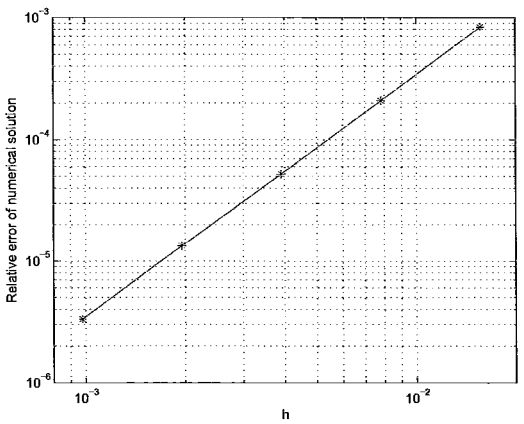

Figure A.3: The order of accuracy of the RK3-CN method is $\mathcal{O}(h^2)$.

Appendix B

Rescaling in Burgers Equation

Recall from the discussion in section 4.4.2, we would like to be sure that the optimization algorithm converges to a global optimizer. To verify this, we initialize it with functions of different wavenumber and compare the corresponding optimal initial condition. We would like to demonstrate that if we solve Viscous Burgers Equation with two different initial data, one being the scaled version of the other, then the solutions to VBE will preserve the spatial scaling, provided we enforce the correct time scaling.

To begin with, consider two different domains $\Omega_1 = [0, 1]$ and $\Omega_2 = [0, 1/L]$. Let $x \in \Omega_1$ and $\xi \in \Omega_2$. Then $x = L\xi$. Let also $v(\xi, \tau) = Lu\left(x(\xi), t(\tau)\right)$ for $\tau = t/L^2$. Then the following holds:

$$\frac{\partial v}{\partial \tau} = L\frac{\partial u}{\partial t}\frac{\partial t}{\partial \tau} = L^3\frac{\partial u}{\partial t}, \tag{B.1}$$

$$\frac{\partial v}{\partial \xi} = L\frac{\partial u}{\partial x}\frac{\partial x}{\partial \xi} = L^2\frac{\partial u}{\partial x}, \tag{B.2}$$

$$\frac{\partial^2 v}{\partial \xi^2} = L^3\frac{\partial^2 u}{\partial x^2}. \tag{B.3}$$

If $u(x, t)$ is a solution of Viscous Burgers Equation, then:

$$0 = \partial_t u + u\partial_x u - \nu\partial_x^2 u = \frac{1}{L^3}\left(\partial_\tau v + v\partial_\xi v - \nu\partial_\xi^2 v\right). \tag{B.4}$$

meaning that $v(\xi, \tau)$ is also a solution of VBE. The enstrophy associated to

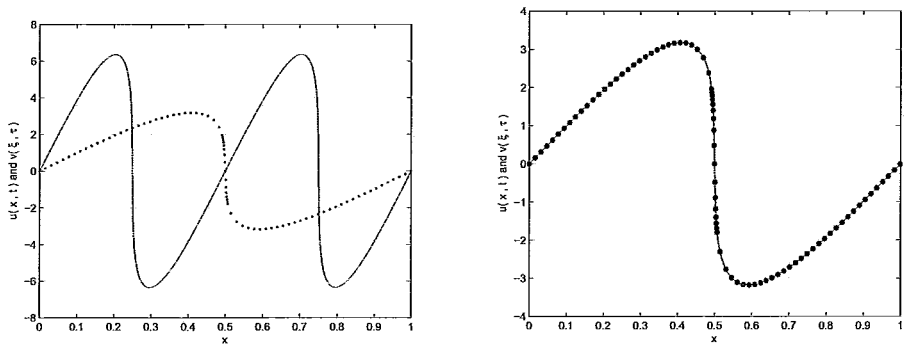

(a) (b)

Figure B.1: (a) Solutions of VBE in the domains $\Omega_1 = [0,1]$ (dotted) and (the extension of) $\Omega_2 = [0,1/2]$ (solid). (b) The two solutions in Ω_1, after rescaling.

solution u is given by:

$$\mathcal{E}_u(t) = \frac{1}{2}\int_0^1 |\partial_x u(x,t)|^2 dx, \tag{B.5}$$

whereas the enstrophy associated to the extension of v into domain Ω_1 is:

$$\begin{aligned} \mathcal{E}_v(\tau) &= L\left(\frac{1}{2}\int_0^{\frac{1}{L}} |\partial_\xi v(\xi,\tau)|^2 d\xi\right) && \text{(B.6)} \\ &= L\left(\frac{1}{2}\int_0^1 L^4 |\partial_x u(x,\tau(t))|^2 \frac{dx}{L}\right) && \text{(B.7)} \\ &= L^4 \mathcal{E}_u\left(\tfrac{t}{L^2}\right). && \text{(B.8)} \end{aligned}$$

Figure B.1 shows the functions $u(x,t)$ and $v(\xi,\tau)$ for $L = 2$ and $t = 0.05$. The enstrophy of the initial condition associated to u is $\mathcal{E}_u(0) = 100$, which sets the enstrophy of the initial data associated to v to $\mathcal{E}_v(0) = 1600$, by the rescaling explained before. The solutions agree perfectly in the domain Ω_1 after the rescaling is applied, as shown in part (b).

Bibliography

[1] T. R. Bewley. *Numerical Renaissance.* Renaissance Press, 2009.

[2] J. F. Bonnans, J. C. Gilbert, C. Lemaréchal, and C. A. Sagastizábal. *Numerical Optimization. Theoretical and Practical Aspects.* Springer, 2003.

[3] C. Canuto, A. Quarteroni, Y. Hussaini, and T. A. Zang. *Spectral Methods.* Scientific Computation. Springer, 2006.

[4] C. R. Doering. *Applied Analysis of the Navier-Stokes Equations.* Cambridge Text in Applied Mathematics. Cambridge University Press, 1995.

[5] C. R. Doering. The 3D Navier-Stokes Problem. *Annual Review of Fluid Mechanics*, 2009.

[6] C. L. Fefferman. Existence and smoothness of the Navier-Stokes equation. `http://www.claymath.org/millennium/Navier-Stokes_Equations/navierstokes.pdf`.

[7] M. D. Gunzburger. *Perspectives in Flow Control and Optimization*, chapter 2. Advances in Design and Control. SIAM, 2003.

[8] H.-O. Kreiss and J. Lorenz. *Initial-Boundary Value Problems and the Navier-Stokes Equations*, volume 47 of *Classics in Applied Mathematics.* SIAM, 2004.

[9] L. Lu. *Bounds on the enstrophy growth rate for solutions of the 3D Navier-Stokes equations.* PhD thesis, University of Michigan, 2006.

[10] L. Lu and C. R. Doering. Limits on Enstrophy Growth for Solutions of the Three-dimensional Navier-Stokes Equations. *Indiana University Mathematics Journal*, 57:2693–2727, 2008.

[11] R. K. Miller and A. N. Michel. *Ordinary Differential Equations.* Dover Publications, 1982.

[12] J. Nocedal and S. J. Wright. *Numerical Optimization.* Springer Series in Operations Research. Springer, 1999.

[13] R. Peyret. *Spectral Methods for Incompressible Viscous Flow*, volume 148 of *Applied Mathematical Sciences.* Springer, 2002.

[14] W. H. Press, B. P. Flannery, S. A. Teukolsky, and W. T. Vetterling. *Numerical Recipes.* Cambridge University Press, 1986.

[15] B. Protas. Adjoint-based optimization of PDE systems with alternative gradients. *Journal of Computational Physics*, 2008.

[16] E. M. Stein and R. Shakarchi. *Real Analysis. Measure Theory, Integration and Hilbert Spaces*, volume 3 of *Princeton Lectures in Analysis.* Princeton University Press, 2005.

[17] L. N. Trefethen. *Spectral Methods in Matlab.* SIAM, 2000.